Detection of Connective Tissue Disorders from 4D Aortic MR images using Independent Component Analysis

Michael Sass Hansen

Kongens Lyngby 2006

Technical University of Denmark
Informatics and Mathematical Modelling
Building 321, DK-2800 Kongens Lyngby, Denmark
Phone +45 45253351, Fax +45 45882673
reception@imm.dtu.dk
www.imm.dtu.dk

Abstract

The current report concerns methods of early detection of connective tissue disorders leading to aortic aneurysms and dissections. Automated and accurate segmentation of the aorta in 4D (3D + time) MR image data is reviewed, and a computer-aided diagnosis (CAD) method using independent component analysis is reported. This admits the objective identification of subjects with connective tissue disorders from 4D aortic MR images.

The majority of the presented work is concentrated on independent component analysis(ICA), estimating sources to be used for the diagnosis task. Prior knowledge of the source distribution is utilized using an ordering of the components. Two new ordering measures are introduced in current work. A novel approach to constrained dimensionality reduction in ICA is developed. A new idea of time-invariant independent components is introduced, and assists in the disease detection in the presence of sparse data.

4D MR image data sets acquired from 21 normal and 10 diseased subjects are used to evaluate the efficiency of the method. The automated 4D segmentation result produces accurate aortic surfaces. The ICA results are validated by a leave-one-out classification test, and are further substantiated by visual inspection of the components. Using a single phase of the cardiac cycle, 8 out of 10 diseased subjects are identified and the specificity is 100 %, classifying all 21 healthy subjects correctly. These results are obtained using components showing correspondence to clinical observations. With 4D information included, the CAD method classifies 9 out of 10 diseased correctly, and still the specificity is 100 %.

Resumé

Den indeværende rapport vedrører metoder til tidlig detektering af bindevævssygdomme, som fører til aortic aneurysms og dissections. En automatisk og præcis metode til segmentering af aorta i 4D (3D + tid) MR data er refereret og en computerassisteret diagnose (CAD) metode, der involverer brugen af independent component analysis, er rapporteret. Dette muliggør en objektiv identificering af subjekter med bindevævssygdomme, udfra 4D MR billeder af aorta.

Hovedparten af det fremlagte arbejde er koncentreret omkring independent component analysis (ICA), som estimerer kilder, der bruges under diagnose opgaven. A priori viden om kildernes fordeling er udnyttet til udformningen af en sortering af de fundne komponenter. To nye sortereringsmål er fremført i det indeværende arbejde. En ny tilgang til dimsionsreducering under bibetingelser i ICA er udviklet. Et nyt koncept om en tidsinvariant independent component er desuden introduceret, hvilket assisterer til sygdomsdetekteringen, når der kun er en stærkt begrænset mængde data til rådighed.

4D MR billedsæt, optaget af 21 normale og 10 syge subjekter, er brugt til at evaluere effektiviteten af den udviklede metode. Den automatiserede 4D segmentering giver en nøjagtig aorta overflade. ICA resultaterne er valideret ved en leave-one-out klassificeringstest, og er yderligere underbygget ved visuel inspektion af de fundne komponenter. Ved brug af en enkelt fase a hjertecyklen, bliver 8 af 10 syge subjekter korrekt identificeret og specificiteten er 100 %, så alle 21 sunde subjekter bliver klassificeret korrekt. Disse resultater er opnået med komponenter, der viser lighed med kliniske observationer af bindevævssygdomme. Når 4D informationen er inkluderet, kan CAD metoden klassificere 9 af 10 syge subjekter korrekt, samtidig med at specificiteten stadig er 100 %.

Preface

This thesis was prepared at Seamans Center of Engeering, the University of Iowa, in fulfillment of the requirements for acquiring the masters degree in engineering. The majority of the work and the writing of one article has been performed in Iowa. The report and the second article were written at the Technical University of Denmark.

This thesis is concerned with analysis of the aortic shape using independent component analysis to diagnose subjects with connective tissue disorders. The main focus of the work has been to address the problem that only data from a limited number of subjects is available.

The thesis consists of a report thouroughly explaining the main conclusions and a collection of the two research papers written during the project period, one published by CVAMIA'06 (App. C) and the other submitted to MICCAI (App. D) awaiting review.

Lyngby, Marts 2006

Michael Sass Hansen

Papers

Here is a list of papers produced during my work with the thesis. Abstracts are included in the appendix.

[C] Michael Sass Hansen, Fei Zhao, Honghai Zhang, Nicholas E. Walker, Andreas Wahle, Thomas Scholz and Milan Sonka. Detection of Connective Tissue Disorders from 3D Aortic MR Images Using Independent Component Analysis *CVAMIA'06, Springer LNCS*, 2006. Accepted for publication.

[D] Michael Sass Hansen, Fei Zhao, Honghai Zhang, Bjarne K. Ersbøll, Andreas Wahle, Thomas Scholz and Milan Sonka. Detection of Connective Tissue Disorders from 4D Aortic MR Images Using Independent Component Analysis *submitted to MICCAI'06*, 2006. Awaiting review.

Acknowledgements

I thank my supervisor Bjarne Kjær Ersbøll for great assistance in structuring my work, and much good advice.

I want to thank my supervisor Milan Sonka for guidance and for giving me inspiration when it was needed. I thank the people from the Medical Imaging group at the University of Iowa for exchanging ideas and letting me be part of the interesting work they are doing. I thank all my new friends in Iowa for having helped making the whole experience of staying in Iowa a great one.

I wish to send a greeting to *Kitware* that provides and keeps improving *The Visualization Toolkit* free of charge. I certainly spent many joyful hours unravelling the mysteries of 3D visualization.

Last I want to thank my girlfriend Camilla for being so supportive and sticking by me during the whole process.

Contents

CHAPTER 1

INTRODUCTION

Aortic aneurysms and dissections are the 15th leading cause of death in the the U.S., representing 0.7 % of all deaths in 2004 [1]. Persons with certain connective tissue disorders, such as Marfan's syndrome and Familial Thoracic Aortic Aneurysm syndrome are at increased risk of developing aortic aneurysm and dissection, which makes an early detection very important.

This study is approaching cardiovascular disease diagnosis using magnetic resonance (MR) imaging. Producing manual outlining of the aorta in 3D images requires expert knowledge and is a tedious and time-consuming task. Detection of connective tissue disorder is based on a crude diameter measure of the ascending aorta from a single 2D MR-slice. Fig. 1.1 shows three 2D slices of a typical 3D cardiac MR images with manually traced aorta contours.

The reported work focuses on the analysis of the automatically segmented aorta. The segmentation was done in a previous study as reported in [2], and the outline of the applied method is provided here for completeness. The data was normalized to 16 phases of the cardiac cycle, and the aortic shapes for three of the cardiac phases are illustrated for a subject in Fig. 1.2. The aortic shapes were analyzed using a point distribution model based on independent component analysis (ICA). The ICA method was extended with two different ordering measures and a novel approach to dimensionality reduction. To utilize the information of all the 16 phases and find statistically significant descriptors, the

Figure 1.1: Three sample 2D slices of a typical aorta candy-cane MR image with manually traced contours outlining aortic lumen.

concept of dividing the model into time-invariant and time-variant components has been introduced.

Figure 1.2: The phases 1, 6 and 11 of the cardiac cycle of a healthy subject.

A computer-aided diagnosis (CAD) method for objective identification of subjects with connective tissue disorders from 16-phase, 3D+time aortic MR images using independent component analysis is reported.

1.1 Organization of the report

The report is divided in four parts, each described below.

- **Background (I):** The imaging technique is described, as well as some of the connective tissue disorders and the most common effects they may cause. The data is presented as well as previous work in the area.

- **Methods (II):** The proposed automatic 3D segmentation method is reviewed and the concept of a point distribution model is described. Independent component analysis (ICA) is described along with associated algorithms and the development of several extensions to the basic ICA model is presented. The structure of the implemented program is shortly described.
- **Results (III):**. The segmentation results are demonstrated, and the estimated indpendent components are evaluated both by visual inspection, and by performing a classification task on the labeled subjects.
- **Discussion and conclusion (IV):** The developed methods are discussed as well as the obtained results.

Part I

BACKGROUND

Outline of the presented background

In this part of the report the background of the study is summarized. Both the physical background of MR imaging and the clinical background of the connective tissue disorder are reviewed. In chapter 2 the development of cardiovascular MR imaging is presented, including the basic physics and a description of the state of the art techniques. Chapter 3 contains a review of connective tissue disorders including a description of current diagnostic techniques. Chapter 4 presents the available data and gives an outline of the problem at hand. The recent contributions in the fields of this thesis are outlined in chapter 5.

CHAPTER 2

Cardiovascular Magnetic Resonance Imaging

The first steps towards cardiovascular magnetic resonance imaging were taken back in the early 1980's but huge advancements have been made since then. Magnetic resonance imaging (MRI) is based on the physical principles of nuclear magnetic resonance (NMR). Almost every nucleos in the periodic system has a net spin due to an unpaired proton or neutron [3]. This spin causes the nucleus to function like a tiny magnet. In order to minimize the energy, the spin tends to align with an external magnetic field, while the axis is still rotating around the magnetic field. This is illustrated in Fig. 2.1

The rotation around the magnetic field can be amplified by applying an oscillating electric field at the resonance frequency. Once the oscillating field is removed, the nuclei falls back into the normal state, shown in Fig. 2.1. This is the basic principle behind NMR. The more recent techniques use a gradient in the magnetic field and a whole range of frequencies to assemble an image in the fourier space. Fourier transformation gives the images as they are presented in this thesis.

MRI technique has advantages such as high spatial and temporal resolutions, and favorable signal-to-noise ratio. It is widely used in routine clinical practice. Approximately 200 million MRI scans were in 2004 reported performed on more

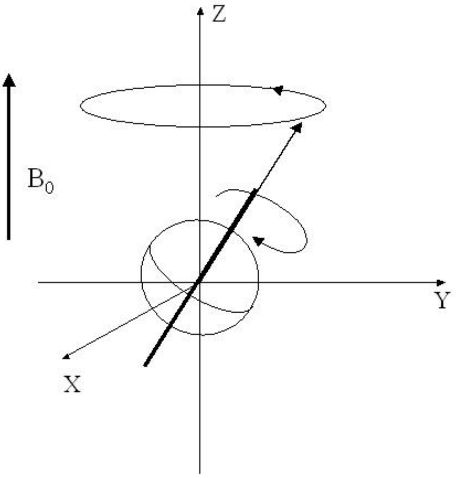

Figure 2.1: This spin axis tend to align with the magnetic field, while still revolving around the magnetic axis.

than 20,000 MRI units worldwide [4]. Protocols focused on imaging of the heart region are referred to as Cardiovascular Magnetic Resonance (CMR).

The CMR images are typically 4D images acquiered using an ECG signal to trigger the data acquisition. The cardiac cycle is defined at the period of time between two peaks of the ECG R-wave. A simple ECG graph is shown in Fig. 2.2. The basic principle of ECG measurements is to measure the depolarisation of cells in the heart, which happens at every heartbeat.

The CMR images are acquired from a slice of the 3D object of interest. To reduce scan time and achieve desired temporal resolution, the slice thickness is normally chosen larger than the slice plane resolution. A typical voxel size of a 3D CMR image is 1.5mm×1.5mm×8mm, where 8mm is the slice thickness and 1.5mm is the slice plane resolution. The 3D image representation of the whole object of interest is acquired by stacking several slices of CMR images and the resulting 3D image is therefore anisotropic in 3D. The stacking process is illustrated in Fig. 2.3.

A 4D image representation of the object of interest is acquired from several cardiac cycles. The typical procedure of acquiring a 4D image with a fixed number of phase, N, is to measure the current cardiac cycle length and calculate the time offsets for each phase. During a whole cardiac cycle, the images are acquired from one or several slices at fixed locations at calculated time offsets.

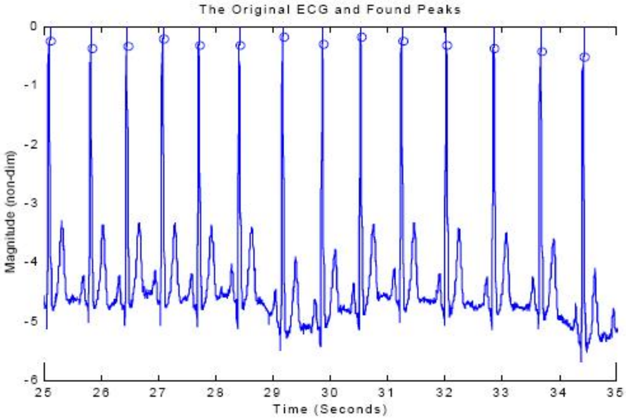

Figure 2.2: A sample of an ECG signal with the the R-wave peaks illustrated with circles. Adapted from [5]

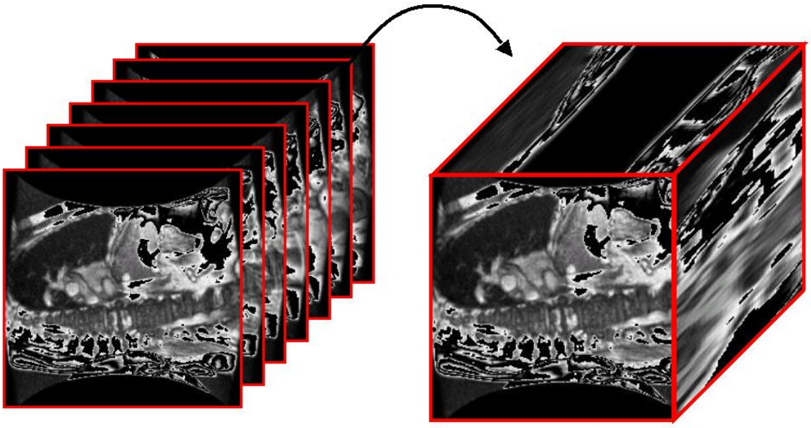

Figure 2.3: An illustration of the merging of several slices into a volume.

This step is repeated to acquire images at different slices until images from all prescribed slices are acquired. Images can be taken with a lot of different views, including short axis and long axis views that refers to the axes of the heart.

Several typical artifacts of the CMR images are:

- The anisotropic nature of voxel may introduce partial volume effect, a loss of resolution caused by multiple features present in the image voxel. For example, a voxel may contain both water and fat and the resulting image pixel intensity is neither of fat nor of water.
- The motion artifact is caused by motion of the entire object or part of it during acquisition. It typically results in blurring of images.
- Flow artifact caused by flowing blood or fluids in the body.

Chapter 3

Connective Tissue Disorders

The connective tissue supports many parts of the body like the skin, the eyes, the heart and the skeletal system. The connective tissue disorders can affect all these different parts. The most significant of the defects are cardiovascular abnormalities, which may include enlargement or dilatation of the base of the aorta, with aortic regurgitation, and prolapse of the mitral valve. People affected with connective tissue disorders have high risk of developing aortic aneurysm and dissection, described in section 3.1 and section 3.2 [6]. Congenital connective disorders include Chondrodysplasias, Cutis Laxa, Ehlers-Danlos Syndrome, Marfan's Syndrome, Mucopolysaccharidoses, Osteogenesis Imperfecta, Osteopetroses and Pseudoxanthoma Elasticum [7].

People with the Marfan's syndrome carry a mutation in one of their two copies of the gene that encodes the connective tissue protein fibrillin-1. The majority of the affected individuals (75%) have inherited an abnormal copy of this gene from an affected parent. About one-quarter of the affected people have a new mutation that is not present in anyone else in their family but can be passed to their offspring [9].

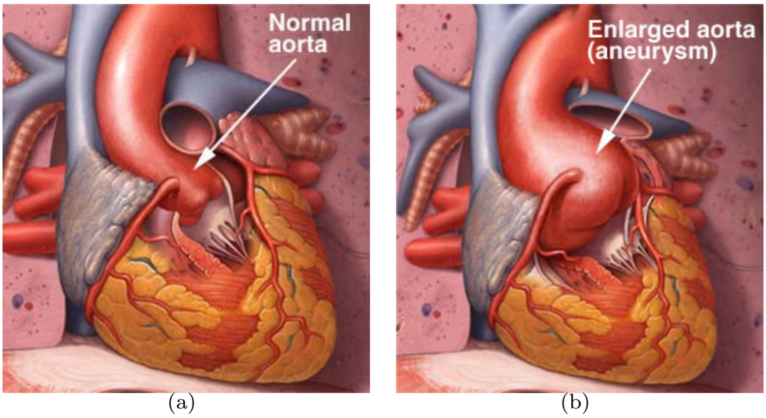

(a) (b)

Figure 3.1: The effect of Marfan's syndrome on the aorta adapted from [8]. (a) A normal aorta. (b) An aorta with enlargement caused by Marfan's syndrome.

3.1 Aortic Aneurysm

Aortic aneurysm [6] is a localized abnormal expansion, widening or ballooning of the aorta wall. Congenital connective tissue disorders such as Marfan's syndrome, trauma, and less commonly, syphilis, hardening of the arteries (atherosclerosis) and high blood pressure (hypertension) can lead to aortic aneurysm. Aortic aneurysms occur in the ascending aorta (25 % of the time), the aortic arch (25 % of the time), or the descending aorta (50 % of the time). An example of ascending aorta aneurysm is shown in Fig. 3.1 . Aneurysms are potentially dangerous because they may burst [10].

Patients with aortic aneurysms are treated if the diameter of the aorta is greater than 5 - 6 cm. Because the size of individuals differ, an aneurysm may also be defined by how much larger the weak area of the aorta is, compared to its normal size for that person. If the enlarged area is 1.5 to two times larger than the normal size of the blood vessel, it is defined as an aneurysm [11]. A common treatment is to surgically replace the aorta with a fabric substitute. For smaller aneurysms of the descending aorta, the aorta can be stented by placing a tube inside the vessel without chest incision or introducing specialized catheters through arteries at the groin. Operation puts the patient under high risk of complications which may include: heart attack, irregular heartbeats, bleeding, stroke, paralysis, graft infection, and kidney damage. Death soon after the operation occurs in 5 - 10 % of the patients.

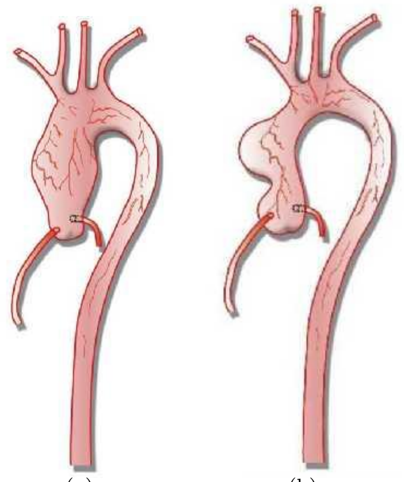

(a) (b)

Figure 3.2: The two typical shapes of an aortic aneurysm adapted from [11]. Both aneurysm are illustrated on the ascending aorta. The three blood vessels, at the top of the aorta, are positioned at the aortic arch, and the descending aorta is the long part descending. (a) Fusiform aneurysm, which is an area enlarged in all directions. (b) Saccular aneurysm (below right), which is a bulge or sac on one side of the aorta

3.2 Aortic Dissection

Aortic dissection [12] involves tearing of the inner layer of the aortic wall. As a result a new false channel forms in the wall of the aorta. The likelihood of death within the first 48 hours is 1 % per hour for untreated patients. The disorder is curable with surgical repair if it is performed before aortic rupture. Less than half of the patients with ruptured aorta survive.

A dissecting aneurysm indicates that the inner wall of the aorta develops a tear which propagates down the inside of the aorta due to the blood pressure. It may also be associated with other injury, infection or congenital weakness of the aorta such as Marfan's syndrome.

Chapter 4

Data description

The presented research is part of a study on Highly Automated Analysis of 4-D Cardiovascular MR Data funded by an NIH grant provided for the medical imaging group at the Department of Engineering, University of Iowa [13]. The goal of the project is in part to create ”A set of validated quantitative indices of aortic morphology and motion”. The subjects investigated in the current study are 10 patients, genetically known to have a connective tissue disorder, and 21 normal persons scanned for the purpose of comparison. The patients and the test subjects are as far as possible drawn from the same demographic distribution.

The analyzed MR data is acquired by either Siemens or GE MR scanners. The sequences used are Fiesta for the GE scanner and True Fisp for the Siemens scanner. Those sequences are virtually identical, so no bias caused by the used scanner is expected. The images are of two standard views, the candy cane view and the left ventricluar outflow tract (LVOT) view. This is because the second one is normally used in the manual diagnosis of connective tissue disorders, because it gives more accurate images of the ascending aorta. They are both visible in Fig. 4.1.

In Fig. 4.2 more data is illustrated for inspection.

The original voxel size for the GE scanner is $1.5 \times 1.5 \times 6\text{mm}^3$ with image size

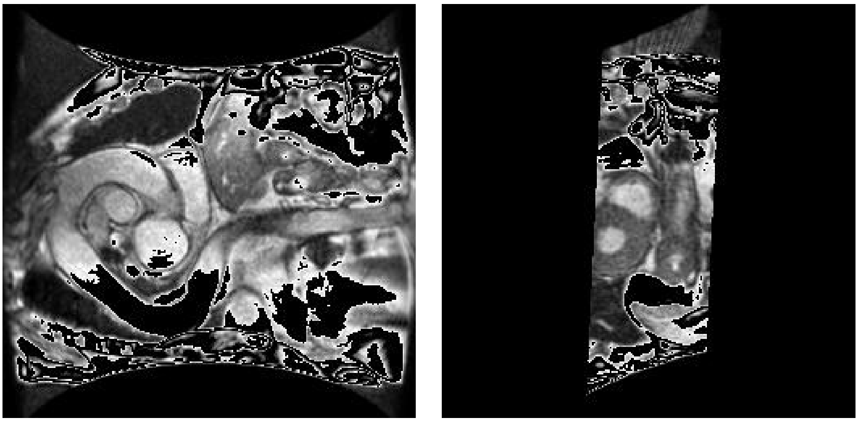

(a) (b)

Figure 4.1: Images representing the two different views present in the acquired set of data. (a) Candy cane view. (b) Left ventricular outflow tract view.

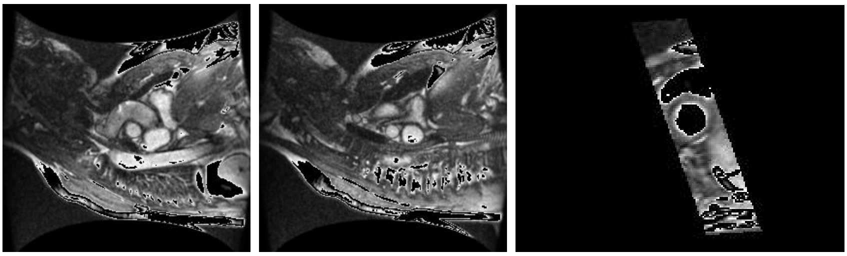

Figure 4.2: Three typical images of the acquired dataset.

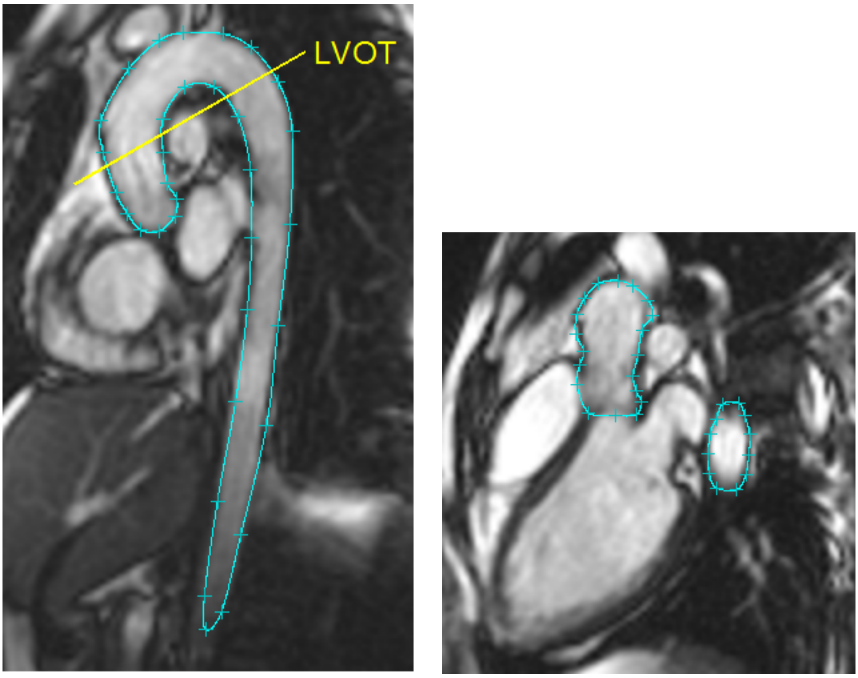

(a)

(b)

Figure 4.3: Images demonstrating the registered images to be merged to create the data ready for analysis (a) Candy cane view. (b) Left ventricular outflow tract view.

256×256. The voxel size for the Siemens scanner is about $1.9 \times 1.9 \times 6\text{mm}^3$ with image size 132×192. Typically 15–25 phases were acquired per cardiac cycle, together forming the 4D data. The 4D data is created by interpolating (using nearest neighboring) the anisotropic images into isotropic images and merge the images from candy cane and LVOT views together after registration as can be seen in Fig. 4.3. It can be seen that the two different images desribe the same area of the body, and they are merged to give data with fewer artifacts and less noise.

The number of phases of the cardiac cycle is normalized to 16 using cubic B-spline interpolation. The resulting preprocessed data consist of 4D data with 16 phases. Part of the analysis consists of segmenting the aorta. The aorta is visible in Fig. 4.1(a) as a candy cane or a bit like a question mark tilted left. Typical examples of the aorta can be seen in Fig. 4.4, where the mean of all the diseased subjects and of the healthy subjects are illustrated. The mean of the diseased (Fig. 4.4(b)) is seen to be a bit dilated compared to the mean of the healthy subjects (Fig. 4.4(a)), which corresponds to clinical observations refered to in section 3. The mean shape is unfortunately not precise enough, as a descriptor, to separate the two classes using a simple distance measure or canonical discriminant analysis. This is part of the motivation for the current work. Examples of the segmented aorta are available in App. A.

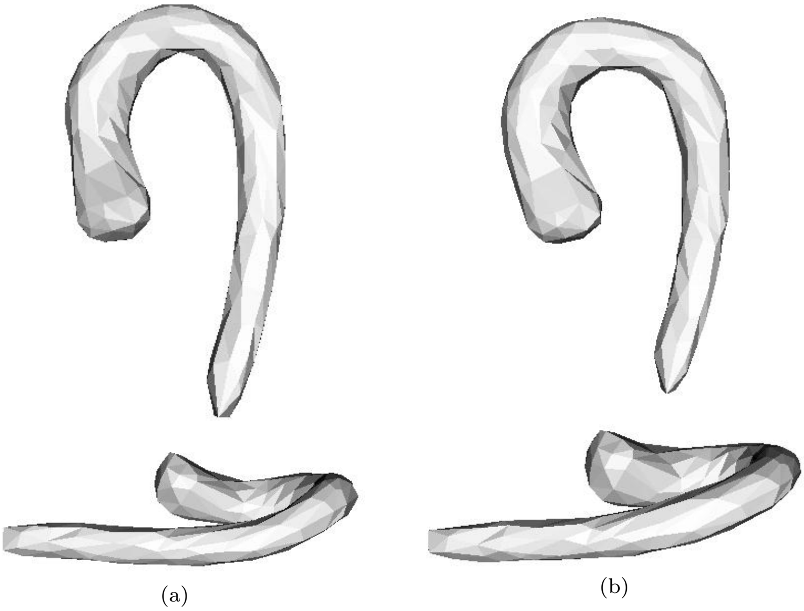
(a) (b)

Figure 4.4: Mean shape of healthy versus diseased subjects, taken over the first phase of the cardiac cycle from all the subjects. (a) The mean shape of all healthy subjects. (b) The mean shape of all diseased subjects.

Chapter 5

Previous work

The aortic segmentation of computed tomography (CT) and MR images has already undergone a lot of research. Due to the labor intensive and difficult analysis of the vast amount of images, developing reliable and fast analysis tools has been a high priority for a decade. Rueckert et al. [14] used Geometric Deformable Models (GDM) to track the ascending and descending aorta. Behrens et al. [15] obtained a coarse segmentation using Randomized Hough Transform (RHT). Bruijne et al.[16] introduced an Adapting Active Shape Models (ASM) for tubular structure segmentation. Subasic et al.[17] utilized the level-set algorithm for segmentation of abdominal aortic aneurysm (AAA). Though aortic segmentation has been repeatedly attempted in the past, it is believed this is the first study investigating its use for connective tissue disorders detection.

Independent component analysis (ICA) has its origin in the 1980's in the area of neurophysiology and was soon adapted in neural network applications by Herualt et al. [18]. Not untill the 90's did the area recieve much attention outside of France and with the development of the *fastICA* algorithm in 1997 by Hyvärinen et al.[19], it is now a mature active field of research. Lelieveldt et al.[20] have studied the application of ICA in statistical shape models, instead of the more commonly used PCA. ICA has proved to be a well suited tool in the analysis of the myocardial diseases. In modelling the left ventricular myocardial contour, ICA extracted more localized features that helped to assess the myocardial contractibility patterns [21].

The same data that has been analyzed in the current work was previously analyzed using a support vector machine [2]. This gave good results that were unfortunately very difficult to interpret clinically. The above mentioned features of independent component analysis, in particular in the ventricular modelling was the source of inspiration for applying ICA to the same problem.

Part II

METHODS

Outline of the presented methods

In this part of the report the different methods applyed in the computer aided diagnosis are described. This part is divided in chapters each describing a different of the applied methods. Initially the segmentation algorithm is described briefly in chapter 6, for the purpose of completeness, though the development has not been part of the presented thesis. Chapter 7 gives an introduction to the concept of capturing shape variations in a point distribution model. The theory of independent component analysis is reviewed in chapter 8, including an illustration of the method, which also certifies that the implemented algorithm works as expected. The three subsequent chapters 9, 10 and 11 provide thorough descriptions of the developed extensions of the basic ICA model presented previously. In chapter 12 the classifiers used in the diagnostic step are presented. Chapter 13 describes the structure of the implemented *Visual C++* program.

Chapter 6

Segmentation

The segmentation method is as mentioned previously to provide a complete description of the diagnosis process, from 4D MR images to the final diagnosis. The work has been reported by Zhao et al. [2].

6.1 Aortic surface presegmentation

A 3D fast marching segmentation method [22] was used to obtain an approximate aortic surface. Starting with a small number of interactively identified seed points within the aorta, the initial surface Γ propagates in an outward direction with the speed F. Let $T(x, y, z)$ be the arrival time at which the level set surface passes through the point (x,y,z) in the 3D image. The gradient of this arrival time shall be inversely proportional to the speed function F [22].

$$|\nabla T|\, F = 1 \tag{6.1}$$

The principal idea behind fast marching methods is to trace the surface according to the solution function $T(x, y, z)$ solved using Eq. 6.1. To facilitate numerical solution, discretization in both space and time domains must be performed. Then,

$$\begin{bmatrix} max\left(D^{-x}_{i,j,k}T, 0\right) + min\left(D^{+x}_{i,j,k}T, 0\right) \\ max\left(D^{-y}_{i,j,k}T, 0\right) + min\left(D^{+y}_{i,j,k}T, 0\right) \\ max\left(D^{-z}_{i,j,k}T, 0\right) + min\left(D^{+z}_{i,j,k}T, 0\right) \end{bmatrix}^{1/2} = \frac{1}{F_{i,j,k}} \tag{6.2}$$

where D^+ and D^- represent forward and backward difference operators. The speed function is defined by Eq. 6.3, where $G_\sigma * I_{x,y,z}$ represents the image smoothed by a Gaussian filter with a characteristic width σ. This definition ensures that the surface development stops at a voxel with a high gradient.

$$F(x) = e^{-\alpha|\nabla(G_\sigma * I_{x,y,z})|}, \alpha > 0 \tag{6.3}$$

Using a binary tree sorting technique, the fast marching method can solve Eq. 6.2 with a time complexity of $O(N \log N)$, where N is the number of visited points in the image [22]. The fast marching algorithm stops the surface in the vicinity of object boundaries yielding an approximate object surface.

In order to achieve an accurate segmentation, a skeletonization algorithm [23] is applied to the result of the approximate segmentation to extract the aortic centerline. As a last segmentation step, a cylindrical surface graph search method is used to accurately determine the final luminal surface.

6.2 Accurate aortic surface segmentation

Optimal border detection is an efficient segmentation algorithm applicable to tubular surfaces such as blood vessel. The method consists of 1) a coordinate transformation, 2) surface detection using dynamic programming, 3) mapping of the segmentation result back onto the original image.

Coordinate transformation. In order to construct the aortic surface detection graph, a coordinate transformation is needed. First, cross sections are obtained by resampling the image in the directions perpendicular to the centerline. Each voxel in the aortic cross sections is resampled using a cubic B-spline interpolation technique [24, 25]. The aorta is straightened by stacking the resampled cross sections to form a new volume. Each cross section in the resampled volume is unfolded into polar coordinates to transfer the cylindrical surface into a terrain-like surface [26]. This unfolded image is used for construction of the aortic surface detection graph. Fig. 6.1 shows the process of straightening the aorta into a cylindrical tube. Fig. 6.2 shows the unfolding process.

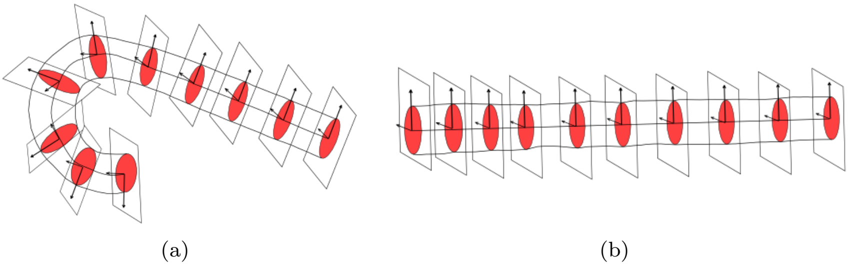

Figure 6.1: The process of transforming the aorta into a straight cylinder.

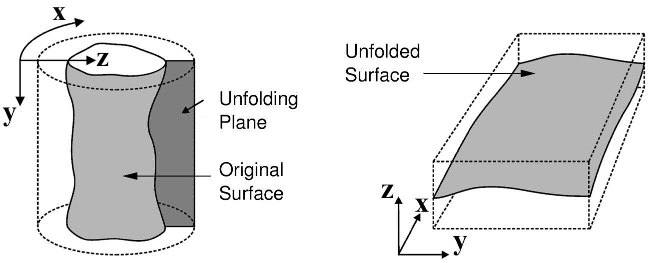

Figure 6.2: Unfolding of the cylindrical surface into a terrain-like surface.

Detection of the accurate surface. After constructing the graph from the unfolded cross-sections, the border detection problem is transformed into a search for optimal paths in weighted graphs [26]. Each pixel in the unfolded cross section corresponds to a node in the graph. A cost is assigned to each node. The lower the cost, the more likely it is that the node is actually on the border. The minimum-cost path (optimal border) that connects the start node and the end node is determined by dynamic programming [26].

Cost function design. The cost functions used for the identification of the aortic surfaces plays a vital role in the graph search methods. Since the ascending aorta is connected to the left-ventricle and is surrounded by tissue of similar MR appearance as the aortic wall, the borders of ascending aorta are hard to detect with a simple cost function. In this study, two different cost functions were developed – one for the ascending aorta and the second for the descending aorta. First, a 3D edge image of the aorta is formed. The usual simple edge operators often overestimate or underestimate the actual border positions. To overcome this problem, our edge operator utilizes a combination of first and second derivatives (3 × 3 Sobel edge detector and 5 × 5 Marr-Hildreth edge detector) of 2D gray-level images [27]. The edge image can be represented by:

$$E = (\alpha S + \beta M) I \ , \tag{6.4}$$

where I is the original image, S is the Sobel operator, and M is the Marr-Hildreth operator. The parameters α and β control the relative weight of the first and second derivatives. In the results presented in this study, α was fixed at 0.8 and $\beta = 0.2$. The cost function can be represented as:

$$C(i,j) = \max_{x \in X, y \in Y} \{\bar{F}(x,y) - \bar{F}(i,j)\} \ , \tag{6.5}$$

where $\bar{F}(i,j)$ is the edge function which is "inverted" to form the cost function.

- Descending Aorta and Aortic Arch: Let $d(i,j)$ represent the edge direction of a pixel (i,j). The edge function for the descending aorta and the aortic arch is as follows:

  $$\bar{F}(i,j) = \begin{cases} E(i,j) & d(i,j) \in [\pi/2, 3\pi/2] \\ E(i,j) - \Delta P & \text{otherwise} \end{cases} \tag{6.6}$$

  where ΔP is a constant penalty term.

- Ascending Aorta: The ascending aorta borders are difficult to detect with a simple cost function such as given in Eq. 6.6. In order to overcome this problem, a knowledge-based cost function [28] is used for the ascending part. After examining the cross section perpendicular to the centerline, a small gap between the ascending aorta border and its surrounding tissue was detected (Fig. 6.3). The thickness of this gap ranged from 2 to 4 pixels. Using this information, the edge function of the ascending aorta is calculated as a combination of two related edges:

  $$\bar{F}(i,j) = \bar{F}_i(i,j) + \bar{F}_o(i,j) \tag{6.7}$$

  The inner edge function $\bar{F}_i(i,j)$ and outer edge function $\bar{F}_o(i,j)$ are:

  $$\bar{F}_i(i,j) = \begin{cases} E(i,j) & d(i,j) \in [\pi/2, 3\pi/2] \\ E(i,j) - \Delta P & \text{otherwise} \end{cases} \tag{6.8}$$

  $$\bar{F}_o(i,j) = \max_{\Delta j = 2,3,4} \begin{cases} E(i,j+\Delta j) & d(i,j+\Delta j) \in [-\pi/2, \pi/2] \\ E(i,j+\Delta j) - \Delta P & \text{otherwise} \end{cases} \tag{6.9}$$

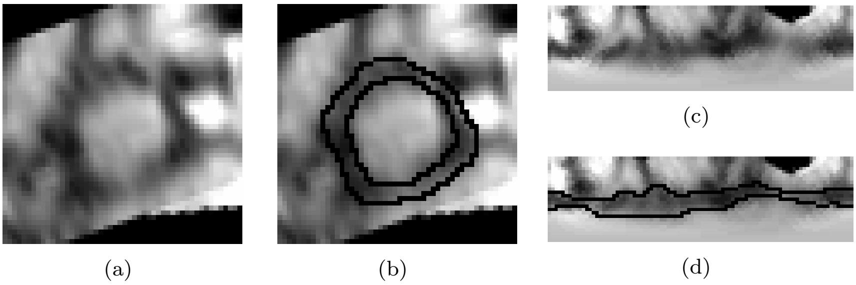
(a) (b) (c) (d)

Figure 6.3: (a) A single 2D cross section of the ascending aorta. (b) the cross section with manually traced outlines. The inner outline is the border of ascending aorta, the outer outline is the border of the surrounding tissue. (c) The unfolded image of (a). (d) The unfolded image with manually traced outlines. The lower outline is the border of ascending aorta, the upper outline is the border of the surrounding tissue.

Chapter 7

Point Distribution Model

Using the segmentation results, a shape Point Distribution Model (PDM) of the aorta population was generated. A PDM serves to represent shapes as variations over a mean shape. Building the PDM consists of two stages: 1) Automatic generation of aortic landmarks on the 3D segmentation result. 2) Capturing the shape variation by using statistical shape analysis, namely independent component analysis on the aortic shape.

7.1 Landmark generation

To build the PDM, the shape must be described by n corresponding landmarks. In this study, we generated the landmarks automatically from the aortic segmentation results in the following 3 steps:

1. *Template shape generation.* In order to obtain a compact model, the segmentation result images were aligned to remove the Euclidian transformation effects of scale, rotation and translation by applying an affine transform T_{affine}. The template shape was generated by applying shape-based blending [29] to the aligned segmentation surfaces.

2. *Template Shape landmarks generation.* Landmarks were generated on the template shape. The general layout of the method for generating landmarks was using triangular meshes to model the surface of the aorta, and use vertices of these triangular meshes as landmarks. A marching cubes algorithm [30] was used to generate the triangular meshes.

3. *Landmarks mapping.* Once the entire set of aortic segmentations was landmarked, each landmark was mapped back onto the original image data. In other words, the landmarks generated on the template shape were mapped back onto the original volumes by using the inverse affine transform T_{affine}^{-1} followed by a B-spline elastic transform to propagate the landmarks onto the individual shapes. Each resulting shape sample was represented by a shape vector $x = (x_1, y_1, z_1, ..., x_m, y_m, z_m)$, consisting of m pairs of (x, y, z) coordinates of the landmark points.

7.2 Shape Analysis

The landmarks were set to have correspondence between the different aortic shapes, in line with their nature. To analyze the different shapes they can be modelled as variations of a golden standard shape. This is much related to the way humans interpret images. For instance if one thinks of an apple, everybody can picture an apple, though apples come in variety of shapes, sizes and even colors, but still we have a clear idea of the concept of an apple. Similarly the shape analysis is based on the analysis of variations over a shape chosen to be the mean shape. The mean shape is estimated as a mean of all the individual shapes. The mean shape for the first phase of the cardiac cycle is illustrated in Fig. 7.1.

Subtracting this mean shape from all samples makes the sample vectors zero-mean, which is an important prerequisit in independent components analysis, used to model the shape variations, as presented in chapter 8.

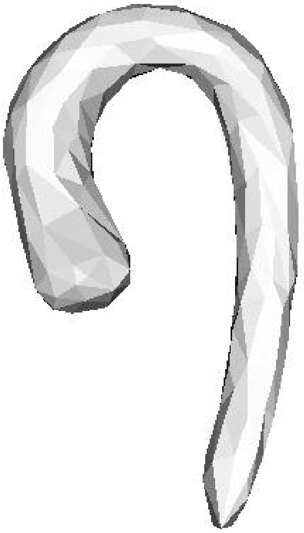

Figure 7.1: The mean shape of the first phase of the cardiac cycle.

Chapter 8

Independent Component Analysis

Independent Component Analysis (ICA) is a method suitable for recovering independent sources that are mixed to form new signals. The general assumption, which has also been adopted in this work, is that the mixing process is linear.

The classical ICA example consists of a setup of several microphones placed at a cocktail party to pick up many distinct voices speaking. Each microphone will receive a different signal, depending on which persons it is close to. In this case ICA is suitable for separating the voices without using any knowledge of speak recognition, except for the fact that the amplitude of the voices is non-Gaussian.

8.1 The Linear ICA model

Linear ICA models assume that the observed signals are linear combinations of the independent sources.

$$X = AS \ , \tag{8.1}$$

where $X_{d\times 1}$ are the d observed signals, $S_{k\times 1}$ represents the value of the k independent sources and $A_{d\times k}$ is the mixing matrix. To correctly identify the true sources $d \geq k$ needs to be true. It might actually be possible to estimate the mixing matrix in cases $d < k$, but the sources can still not be determined, because the mixing matrix $A_{d\times k}$ is not invertible in this case.

To recover the independent sources a *demixing matrix* $W_{k\times d}$ is introduced by

$$S = WX \ , \tag{8.2}$$

where the sources S are assumed of zero mean and unit variance. The true sources can be reconstructed except for a scaling factor.

The independent components can, assuming non-Gaussian distribution of the sources, be found by maximizing a measure of non-Gaussianity. This is due to the Central Limit Theory, which states that a mixture of any two, non-Gaussian, distributions will be more Gaussian than the original distributions. Finding the different components maximizing the non-Gaussianity yields distributions that are not mixtures and the recovered components are thus independent.

8.2 Whitening

Independent component analysis seeks to find components that yield *independent* sources. Unlike principal component analysis nothing can be said about the relation between the variance of these projections. In order to compare two projections the different measures of independence either maximize a measure of non-Gaussianity or a measure of the information content of the sources. Common for all measures is that they deal with the distribution rather than scaling and offset of the variables. For this reason, most algorithms require the data to be *whitened* before the algorithm is applied.

Initially the mean μ is subtracted from the observations to give the input a zero mean. Let $\bar{X}$ denote the data with subtracted mean, then

$$\bar{X} = X - \mu \ . \tag{8.3}$$

The whitening process then consists of a linear transformation that decorrelates the variables and changes the variance of each variable to 1. Let I_d be the unit matrix with dimensions $d \times d$, and U the whitening matrix then

$$\operatorname{cov}(U\bar{X}) = I_d \ , \tag{8.4}$$

where U can be estimated by using principal component analysis, as the principal coefficients are uncorrelated and the analysis also yields the variance of each component for normalizing the variance. Let V be a matrix containing the principal components of $\bar{X}$ and Λ be a diagonal matrix with the variance of each component in the diagonal. The whitening matrix U can be chosen to be

$$U = V\Lambda^{-\frac{1}{2}}V^T \ , \tag{8.5}$$

which, if applied, gives white data as shown by

$$\begin{aligned} \mathrm{cov}(U\bar{X}) &= \mathrm{cov}(V\Lambda^{-\frac{1}{2}}V^T\bar{X}) = V\Lambda^{-\frac{1}{2}}V^T\mathrm{cov}(\bar{X})(V\Lambda^{-\frac{1}{2}}V^T)^T \\ &= V\Lambda^{-\frac{1}{2}}V^T(V\Lambda V^T)V\Lambda^{-\frac{1}{2}}V^T = \Lambda^{-\frac{1}{2}}\Lambda\Lambda^{-\frac{1}{2}} = I_d \ . \end{aligned} \tag{8.6}$$

In general, only a limited number of samples exists in the medical application of independent component analysis. The number of principal values greater than zero equals the number of samples (minus one as the mean has been subtracted). This means that the diagonal matrix with the variances is not invertible, and the above listed scheme can not be applied in this case.

A possible modification giving uncorrelated variables with unit variance will now be presented. Considering each term in the presented matrix $U = V\Lambda^{-\frac{1}{2}}V^T$, the rightmost V^T can be considered as a transformation into a principal coefficient space, $\Lambda^{-\frac{1}{2}}$is a scaling in this space so the variance of the coefficients becomes 1, and the left V a transformation back into the original space. Λ_r is introduced as a reduced version of Λ, where Λ_r is a diagonal matrix where all the r elements of the diagonal are different from zero, including the non-zero principal values of Λ. V_r contains the r corresponding principal components and the singular value decomposition of $\mathrm{cov}(\bar{X})$ can be written $\mathrm{cov}(\bar{X}) = V\Lambda V^T$. Let U_r be the new whitening matrix, then U_r can be written as

$$U_r = \Lambda_r^{-\frac{1}{2}}V_r^T \ , \tag{8.7}$$

giving scaled principal coefficients, all with a variance of one as can be shown by

$$\begin{aligned} \mathrm{cov}(U_r\bar{X}) &= \mathrm{cov}(\Lambda_r^{-\frac{1}{2}}V_r^T\bar{X}) = \Lambda_r^{-\frac{1}{2}}V_r^T\mathrm{cov}(\bar{X})(\Lambda_r^{-\frac{1}{2}}V_r^T)^T \\ &= \Lambda_r^{-\frac{1}{2}}V_r^T(V\Lambda V^T)V_r\Lambda_r^{-\frac{1}{2}} = \Lambda_r^{-\frac{1}{2}}\Lambda_r\Lambda_r^{-\frac{1}{2}} = I_r \ . \end{aligned} \tag{8.8}$$

In this work, the second transformation, U_r, has been used, as it works even when the number of samples is smaller than the number of observed dimensions.

8.3 ICA methods

ICA methods can be split up in two parts, namely an objective function and a optimization algorithm. The ensemble forms an ICA algorithm.
ICA method = Objective function + Optimization algorithm [31].
First different objective functions, typically measuring the degree of non-Gaussianity, are described, and subsequently different optimization algorithms suited for the presented objective functions are treated.

8.3.1 Objective functions

In this section an overview of the considered objective functions is provided.

8.3.1.1 Kurtosis

The Kurtosis kurt(x) of the distribution of a random variable, x, is a measure of Gaussianity. The description of Kurtosis is included in this report because of its simple analytical properties that in section 10.1.1 shall facilitate an analysis of some of the features of independent component analysis. The Kurtosis is defined by

$$\mathrm{kurt}(x) = \frac{\mathrm{E}\{x^4\}}{\mathrm{E}\{x^2\}^2} - 3, \tag{8.9}$$

where x is a random variable. It can be shown that the Kurtosis is 0 for a Gaussian distribution. For practical estimation Kurtosis is far from the optimal measure due to sensitivity to outliers and because it mainly measures the tail of the distribution and is largely unaffected by structure in the middle of the distribution [32]. For the theoretical considerations this does not pose a problem as it can be assumed that the true distributions are know. For two random independent variables x and y it holds that

$$\mathrm{kurt}(x+y) = \mathrm{kurt}(x) + \mathrm{kurt}(y), \tag{8.10}$$

$$\mathrm{kurt}(cx) = c^4 \mathrm{kurt}(x), \tag{8.11}$$

where c is an arbitrary constant. Let the row vector, w, be a projection, wX, on the input data X, and let the projection vector be bound by $\mathrm{E}\{(wX)^2\} = 1$. As stated earlier X is assumed to be generated by the model $X = AS$ (Eq. 8.1). Let z be defined by $z = wA$ and observe that $\mathrm{E}\{(wX)^2\} = wA\mathrm{E}\{S^2\}(wA)^T =$

$\|z\|^2 = 1$, since the sources are independent and assumed of unit variance.

$$\mathrm{kurt}(wX) = \mathrm{kurt}(wAS) = \mathrm{kurt}(zS) = \sum_{i=1}^{k} z_i^4 \mathrm{kurt}(S_i). \tag{8.12}$$

To find distributions diverging from the Gaussian distribution, the numerical value of the Kurtosis can be maximized under the constraint $\|z\|^2 = 1$. This can be shown to be the canonical base vectors $\pm e_i$, projections on only one independent component [33]. Intuitively, remembering the constraint $\|z\|^2 = 1$, it is also expected that maximizing Kurtosis corresponds to distributing the variance over fewer components, as values smaller than one raised to the power of four are reduced even more.

8.3.1.2 ICA by tensorial methods

One approach to ICA can be considered as a generalization of principal component analysis. PCA seeks to maximize the variance of the components, while keeping the correlation coefficients zero. Cumulant tensors are generalizations of the covariance matrix, in particular the fourth order cumulant tensor is given by

$$\begin{aligned}\mathrm{cum}(x_i, x_j, x_k, x_l) = {} & \mathrm{E}\{x_i x_j x_k x_l\} - \mathrm{E}\{x_i x_j\}\mathrm{E}\{x_k x_l\} \\ & -\mathrm{E}\{x_i x_k\}\mathrm{E}\{x_j x_l\} - \mathrm{E}\{x_i x_l\}\mathrm{E}\{x_j x_k\} \ ,\end{aligned} \tag{8.13}$$

which is a four-dimensional array, or a "four-dimensional matrix". All fourth-order cumulants can be obtained as a linear combination of the cumulants of x_i. The Kurtosis, descibed in section 8.3.1.1, of a linear combination of the input, can be written as

$$\begin{aligned}\mathrm{kurt}\sum_i w_i x_i &= \mathrm{cum}\left(\sum_i w_i x_i, \sum_j w_j x_j, \sum_k w_k x_k, \sum_l w_l x_l\right) \\ &= \sum_{ijkl} w_i^4 w_j^4 w_k^4 w_l^4 \mathrm{cum}(x_i, x_j, x_k, x_l) \ .\end{aligned} \tag{8.14}$$

A cumulant tensor is a linear operator defined by the fourth-order cumulants $\mathrm{cum}(x_i, x_j, x_k, x_l)$. The tensor is defined as a linear transformation in the space of $d \times d$ matrices oposed to the covariance matrix with elements $\mathrm{cov}(x_i, x_j)$, which is defined in the space of d-dimensional vectors. Let the transformation of a matrix M be described by $\mathbf{F}$ and the i,jth element be given by the transformation $\mathbf{F}_{ij}$, then the transformation is given by

$$\mathbf{F}_{ij} = \sum_{kl} m_{kl} \mathrm{cum}(x_i, x_j, x_k, x_l) \ . \tag{8.15}$$

As for the common matrix transformation, an eigenvalue decomposition can be defined for cumulant tensor, given by

$$\mathbf{F}(M) = \lambda M \ . \tag{8.16}$$

Assume that a W is found, satsifying the ICA model (8.2) with whitened data, then

$$\bar{X} = W^T S \ , \tag{8.17}$$

since W is orthogonal. $\bar{X}$ then has the special structure that M given by

$$M = \mathbf{w}_m \mathbf{w}_m^T \ , \tag{8.18}$$

is an eigenmatrix, where $\mathbf{w}_m, m = 1, \ldots, d$ is a row of the de-mixing matrix W. This can be shown by considering an element of the transformed matrix.

$$\begin{aligned}\mathbf{F}_{ij}(\mathbf{w}_m \mathbf{w}_m^T) &= \sum_{kl} w_{mk} w_{ml} \mathrm{cum}(\bar{X}_i, \bar{X}_j, \bar{X}_k, \bar{X}_l) \\ = \sum_{kl} w_{mk} w_{ml} \mathrm{cum} &\left(\sum_q w_{qi} S_q, \sum_{q'} w_{q'j} S_{q'}, \sum_r w_{rk} S_r, \sum_{r'} w_{r'l} S_{r'} \right) \\ &= \sum_{klqq'rr'} w_{mk} w_{ml} w_{qi} w_{q'j} w_{rk} w_{r'l} \mathrm{cum}(S_q, S_{q'}, S_r, S_{r'}) \ . \end{aligned} \tag{8.19}$$

Since the sources, S_i, are independent, only terms where $q = q' = r = r'$ gives cumulants different from zero, which gives

$$\mathbf{F}_{ij}(\mathbf{w}_m \mathbf{w}_m^T) = \sum_{klq} w_{mk} w_{ml} w_{qi} w_{qj} w_{qk} w_{ql} \mathrm{kurt}(S_q) \ , \tag{8.20}$$

where it is used that $\mathrm{kurt}(s_q) = \mathrm{cum}(S_q, S_q, S_q, S_q)$. The rows of W are orthogonal which means that $\sum_k w_{mk} w_{qk} = \delta_{mk}$ and the same for index l. This gives

$$\mathbf{F}_{ij}(\mathbf{w}_m \mathbf{w}_m^T) = \sum_q w_{qi} w_{qj} \delta_{qm} \delta_{qm} \mathrm{kurt}(S_q) = w_{mi} w_{mj} \mathrm{kurt}(S_m) \ , \tag{8.21}$$

which shows that matrices of the form (8.18) are eigenmatrices with eigenvalue $\mathrm{kurt}(S_m)$. It can be shown that all other eigenvalues of the tensor are zero [31]. If the eigenvalues of the tensor, corresponding to the Kurtosis of the independent components, are distinct, every eigenmatrix corresponds to one row in the de-mixing matrix W. A method for estimating the desired eigenmatrices is described in section 8.3.2.1.

8.3.1.3 Negentropy and mutual information

Entropy can be percieved as a measure of information or disorder contained in a distribution. If a distribution for example only has two possible states with equal probability the entropy of a random variable distributed according to this distribution is one bit. This is the *information* that is gained if we knew the actual "state" of the variable. It can also be thought of, as the disorder of the variable, in the sense that knowing only the distribution, "how many possible ways" can the variable be distributed. The *differential entropy*, defined for continous valued random vectors Y, is given by

$$H(Y) = -\int p_Y(\epsilon)\text{log}p_Y(\epsilon)d\epsilon \ , \tag{8.22}$$

where p_Y is the density of Y.

The reason that the entropy is an interesting measure in the ICA setting is that among all distributions with a fixed variance, the Gaussian has the largest entropy. This indicates that the difference between the entropy of a distribution and the entropy of a Gaussian distribution with the same variance could be used as a measure of how Gaussian a distribution is. This measure is called negentropy and is given by

$$J(Y) = H(Y_{Gauss}) - H(Y) \ , \tag{8.23}$$

where Y_{Gauss} is a Gaussian random variable. As $H(Y_{Gauss})$ assumes the highest possible value, the negentropy measure is always positive, and maximizing negentropy is in a sense the optimum way of determining non-Gaussianity. The problem though consists of determining the density of the random vector Y. In the presence of sparse data this is very dificult, which is why approximations to the entropy have been introduced.

Another information theoretic approach is minimizing mutual information to recover the independent components which, after approximations, gives the same algorithm for estimating the components.

8.3.1.4 Joint Entropy

Another measure of entropy is the joint entropy, measuring the information contents of a linear projection of the data followed by a nonlinear transformation, which for example can be done by a sigmoid function. The projection Y is then given by

$$Y = f\left[W\bar{X} + w_0\right] \ , \tag{8.24}$$

where w_0 is an extra bias weight. Let $\|J\|$ be the determinant of the Jacobian matrix, then the distribution of the output $Y, p_Y(Y)$ is related to the distribution of the observed signals $p_{\bar{X}}(\bar{X})$ by

$$p_Y(Y) = \frac{p_{\bar{X}}(\bar{X})}{\|J\|} \ . \tag{8.25}$$

The joint entropy is defined similar to the diferential entropy (8.22), except the idea of joint entropy is, as the name implies, to estimate an entropy of the whole de-mixing matrix W, rather than just evaluating a single component. Using the notations introduced already, this can be written as

$$H(Y) = -\mathrm{E}\left[\log p_Y(Y)\right] = \mathrm{E}\left[\log\|J\|\right] - \mathrm{E}\left[\log p_{\bar{X}}(\bar{X})\right] \ , \tag{8.26}$$

where the second term $\mathrm{E}[\log p_{\bar{X}}(\bar{X})]$ is seen to be independent of the chosen weights, which is taken into consideration when maximizing the joint entropy in section 8.3.2.3.

8.3.2 Optimization algorithms

Different algorithms are suited for the different objective functions. This section gives a description of algorithms suited for the presented objective functions.

8.3.2.1 Joint approximative diagonalization of eigenmatrices

The joint approximative diagonalization of eigenmatrices (JADE) method is an approximative method for estimating the eigenmatrices described in section 8.3.1.2. This can be done by restating the eigenmatrix property. The de-mixing matrix W is the matrix that diagonalizes $\mathbf{F}(M)$ for any M. This means that $Q = W\mathbf{F}(M)W^T$ is diagonal. In order to estimate the W's so Q becomes a diagonal matrix a measure is wanted for the amount of diagonalization. An appearent approach is maximization of the diagonal elements, as W is orthonormal and the squared sum of all the elements remains constant.

$$\mathrm{J}_{JADE}(W) = \sum_i \|\mathrm{diag}(W\mathbf{F}(M_i)W^T\|^2 \ . \tag{8.27}$$

In the presence of true and limited data, a complete diagonalization is not possible. The matrices M_i could in principle be chosen arbitrarily, but to reduce computation time, a set consisting of eigenmatrices of the cumulant tensor can be chosen [34]. One problem with the JADE algorithm is that the cumulant tensor scales like $O(n^4)$ with the number of dimensions, so for high dimensionality signals, the memory requirements become very high.

8.3.2.2 FastICA

This algorithm works well with the negentropy (and mutual information) approximation. It does work with several different objective functions, but due to its current use, the negentropy approximation is emphasized, as discussed in App. B

The *FastICA* algorithm is iterative and let n represent the iteration number, $w(n)$ the estimated independent component in the nth iteration step. $X_{d\times 1}$ is a column vector with the d rows representing the observed signals, in the presented case corresponding to features of a patient. The iteration steps are given by the following

$$w(k) = \mathrm{E}\{X^T g(w(n-1)X)\} - \mathrm{E}\{g'(w(n-1)X)\}w(n-1), \tag{8.28}$$

where g and g' are derivatives of a non-quadratic function $G(u) = -\exp(-u^2/2)$. This is the previously mentioned negentropy approximation. The components are found sequentially and the data projected into the subspace orthogonal to the recovered projections to improve performance and convergence [35]. The weight vector, w, is randomly initialized which influences the obtained solution due to multiple local maxima. Multiple w's were initialized allowing the selection of the one resulting in a source with the most desirable properties.

8.3.2.3 Gradient descent

Gradient descent works by maximizing a function iteratively by moving in small steps along the negative gradient untill a suitable maximum is reached. Let G be a function of the weight vector w, then the update rule can be described by

$$\Delta w = \alpha \frac{\delta G(w)}{\delta W}|_{W=W(t-1)} \tag{8.29}$$

Gradient descent on the joint entropy measure The gradient descent algorithm has proven its worth on the joint entropy measure introduced in section 8.3.1.4. It is noted that the determinant of the Jacobian can be rewritten as

$$\|J\| = \left| \|W\| \prod_{i=1}^{d} \frac{\delta Y_i}{\delta \bar{X}_i} \right| , \tag{8.30}$$

and next using (8.29) gives

$$\Delta W = \alpha \frac{\delta H(Y)}{\delta W} = \frac{\delta}{\delta W} \log \|J\| = \frac{\delta}{\delta W} \log \|W\| + \frac{\delta}{\delta W} \log \prod_{i=1}^{d} \left| \frac{\delta Y_i}{\delta \bar{X}_i} \right| . \tag{8.31}$$

The derivative of $\log\|W\|$ can be rewritten as

$$\frac{\delta}{\delta W}\log\|W\| = [W^T]^{-1} \ , \tag{8.32}$$

giving the final and simpler expression

$$\Delta W = \alpha[W^T]^{-1} + (\mathbf{1} - 2Y)\bar{X}^T \ , \tag{8.33}$$

where the nonlinearity is assumed to be sigmoid.

The gradient descent algorithm was implemented on the joint entropy measure revealing similar results as the *FastICA* algorithm on the aortic shape as well as on the simple test, described in section 8.4. It did have a slower convergence though.

8.3.3 Conclusion

For recovering the independent components, the *FastICA* algorithm has been applied in this study, due to its fast convergence and robustness[32]. As mentioned in section 8.3.1.1, the Kurtosis is not very well suited in practical implementations with only a limited number of samples. The JADE algorithm was previously implemented by the current research group, which did not yield satisfactory results. As discussed in section 10.1.1 more sources than samples may exist, and JADE is not well suited for making a selection between interesting components. Gradient descent on a joint entropy measure was implemented, yielding similar results, but later discarded due to slower convergence.

8.4 A demonstration of ICA

The following example works to prove that the produced implementation works to find independent components, as well as to demonstrate the hypothesis of ICA in the presence of the same number of sources as observable signals.

8.4.1 Two independent sources

This example demonstrates that two independent sources can be identified and separated. The two uncorrelated sources have been constructed as a random uniformly distributed signal and a serrated signal shown in Fig. 8.1(a).

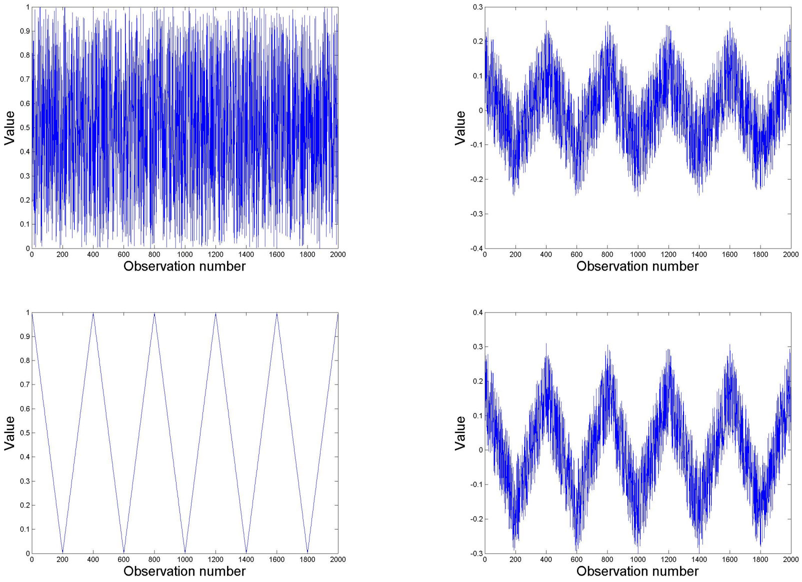

(a) (b)

Figure 8.1: (a) The two indpendent signals. A serrated signal and a random unform signal. (b) Two mixtures resulting from a linear mixture process.

The two signals are mixed linearly using an arbitrary mixing matrix $A_{2\times 2}$ given by

$$A = \begin{bmatrix} 0.23 & 0.30 \\ 0.35 & 0.28 \end{bmatrix}$$

The two signals resulting from the mixture process given by (8.1) are shown in Fig. 8.1(b). It is evident that both mixtures are rather similar mixtures of the sources. Figure 8.2(a) shows a scatter plot of the two sources. It can be seen that both sources are uniformly distributed and in Fig. 8.2(b) it is illustrated how the mixed signals have a skewed distribution.

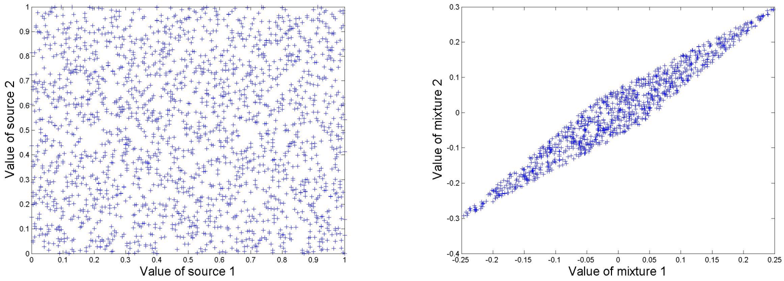

(a) (b)

Figure 8.2: (a) The two indpendent signals. The serrated signal and the random unform signal. Both have a uniform distribution which can clearly be observed in the plot. (b) Two mixtures resulting from a linear mixture process. The uniform distributions are now skewed.

Principal Component Analysis The most common procedure in dimensionality reduction and/or feature extraction is using principal component analysis (PCA). PCA is finding projections that explain the biggest amount of variance, whereas ICA is concerned with finding independent components. In the presence of data with a Gaussian distribution, ICA can not be utilized, as Gaussian distributions can not be distinguished. In this case PCA finds the principal axes in the hyper-ellipsoid describing the Gaussian distribution.

PCA applied on the two mixtures gives two principal axes illustrated in Fig. 8.3(a). It can be observed how the one axis represents the majority of the variation and the other the rest. In describing the two different sources they performed badly, since they are both a mixture of the two independent sources, which can be clearly observed in Fig. 8.3(b).

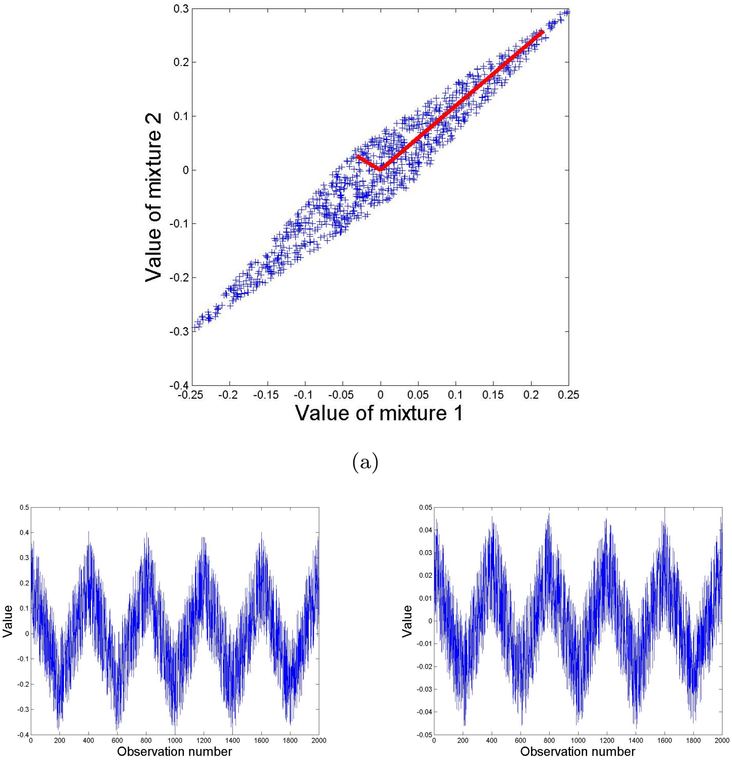

(a)

(b)

Figure 8.3: (a) Scatter plot of the two linear mixtures. The two red lines are illustrating the principal components, scaled like 2 times the standard deviation. (b) The resulting scores of each principal component. The scores on the left graph are from the principal component explaining the most variance, and the scores shown in the right graph are from the other principal component. This can also be observed in the values of the scores, which have greater variance for the first independent component. They are both clearly a mixture of the random uniform signal and the serrated signal.

Independent Component Analysis The obtained results using ICA on the mixed data are presented in this section. Initially the data was whitened as described in section 8.2. Subsequently the *FastICA* algorithm was applied on the whitened data to estimate the independent components. In Fig. 8.4(a) the estimated independent components can be observed. The directions perpendicular to the components have also been emphasized with dashed lines to illustrate that the parts excluded by the projection of the data on the independent components are the other components. In Fig. 8.4(b) the estimated sources can be seen to correspond almost excactly to the true sources illustrated in Fig. 8.1(a), except for an offset and a scaling factor. The amplitude of the sources cannot be determined, as it is unknown if the scaling origins from the mixing process or from the original source signal. A closer investigation yields small ripples in the estimated saw teeth which are caused by chance correlations between the two signals. The average magnitude of these depends on the number of samples.

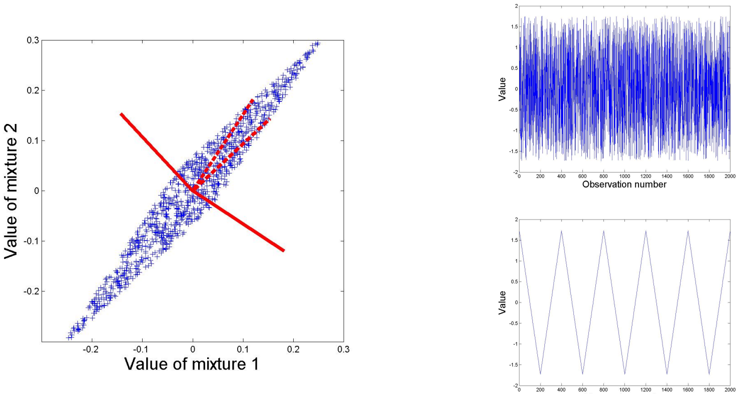

(a)

(b)

Figure 8.4: (a) Scatter plot of the two linear mixtures. The two red lines are illustrating the independent components, scaled apropiately. The dashed lines show the directions perpendicular to the independent components, which can be seen to be directed along the distribution of the other source. (b) The resulting estimated independent sources. It can be seen that the original sources illustrated in Fig. 8.1(a) are reconstructed except for scaling and an offset.

8.5 Conclusion

In this section several objective functions were described as well as some of the optimization algorithms considered. In a previous study, a JADE implementation of ICA by tensorial methods was used, without giving acceptable results. For this reason, this method was not pursued further. The negentropy objective function is analytically attractive, because it in some sense is a ”natural” measure of non-Gaussianity. The approximation introduced in section 8.3.2.2 made for an efficient optimization algorithm. Joint entropy was also an attractive objective function, giving similar results using a gradient descent algorithm, but slower convergence makes the negentropy measure combined with the approximation and *FastICA* algorithm the prefered choice of algorithm. Unless specifically stated, the algorithm used in the remaining of this report is the *FastICA* algorithm as described in section 8.3.2.2, and implemented as outlined in chapter 13.

Chapter 9

A first approach to ICA on the aortic shape

Due to the orthogonalization step in the *FastICA* algorithm, the ordering of the components has a rather great significance on the estimated components. Three different ordering measures are implemented in this work, introducing the new Fisher discriminant measure, a localization measure, and a measure based on the approximated negentropy measure. Section 9.2 introduces the ordering measure that maximizes localization, which is preferable in the interpretation of the extracted components, and in section 9.3 the Fisher discriminant as an ordering measure for extraction of the component that separates the diseased and normals, is described.

9.1 Ordering by the negentropy approximation

Initially the *FastICA* algorithm was applied on the data, searching for the maximum possible number of components that could be estimated. Having 31 subjects, after the whitening process, the maximum number of independent components to be estimated was 30. The coefficient values of the projection of the data onto these 30 independent components yield an initially interesting result. The objective function to be maximized by the *FastICA* algorithm was a measure of non-Gaussianity. In Fig. 9.1 the distribution of the coefficients for each independent component is illustrated.

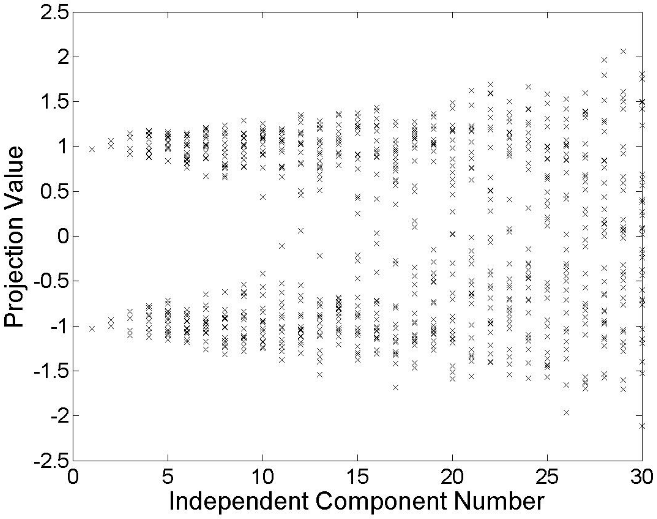

Figure 9.1: Distribution of the projections on each independent component. It can be observed that the first components explain an almost binary division of the patients in two groups.

It is observed that the sources corresponding to the first components are distributed almost solely around the binary values 1 and -1, which gives a very non-Gaussian distribution. Dividing the data into two distinct groups is probably not caused by an underlying feature of the data, but is rather arising from the scarce amount of samples available for estimation of the mean values in the *FastICA* algorithm. The components best suited for distinguishing the normal subjects and the patients, were components of the order 9 - 17, and none showed any particular clear separation between the two groups of subjects. The first component which gives an almost completely binary distribution of the coefficients is shown in Fig 9.2. It can be observed that the major difference between the two binary groups is centered around the ascending aorta, seeming to have two different angles. Also at the tip of the descending aorta there are some differences and this is not a very interesting feature, since the segmentation of the end of the descending aorta is not very robust.

To achieve features with distributions different from just being non-Gaussian, two new ordering measures are introduced.

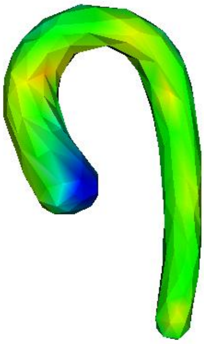

Figure 9.2: Illustration of an independent component. One phase of the independent component is projected onto the mean shape of the aortic candy cane. It is color coded such that red corresponds to a dilation of the aorta at a given point and blue to a shrinkage at that point. Green means the components is not dependent on a point.

9.2 The localization of the components

The true underlying sources are believed to be localized. Being diseased for instance is expected not to influence the entire shape of the aorta, but only a part of it close to the heart at the ascending aorta or at the aortic arch. More generally in medical applications, components are usually expected to show local rather than global features. This is the main reason to reinforce the localization of the enountered independent components through an ordering of the components.

A measure is defined that focuses on the peaks of the shape variation, extending a measure defined by Lelieveldt et al. [20] to 3D. The variation of the shape by a given projection is mapped onto the normals of the mean surface. The normals are determined from the triangulation using a scheme as depicted in Fig. 9.3. Each triangle is assigned a ”spin”, and by registering the spin in each connection between points, forming the triangles, it can be made sure that all the spins are rotating in the same direction. This is done by noting that each edge is an edge in two triangles, and that the ”spin-direction” of the edge is opposite for the two triangles. Starting by assigning a direction to one triangle, the rest can be assigned using this scheme. The normals are found by taking the cross product of two of the edge vectors, using the spin direction to choose the ordering.

The volume between the two triangles, illustrated in Fig. 9.4, is calculated by

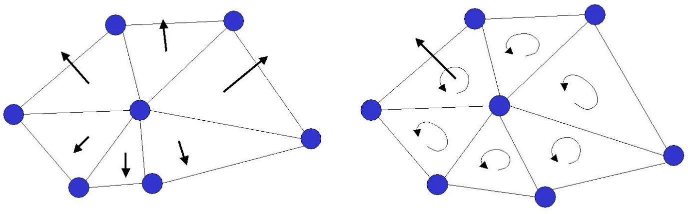

(a) (b)

Figure 9.3: (a) An example of triangles with normals, all pointing in the same direction (either outwards or inwards). (b) Defining a direction by assigning a spin to each triangle.

multiplying the area of the triangle by a projection of the displacement on to the normal vector of the mean shape. All volumes are compared and peaks are found as will be described.

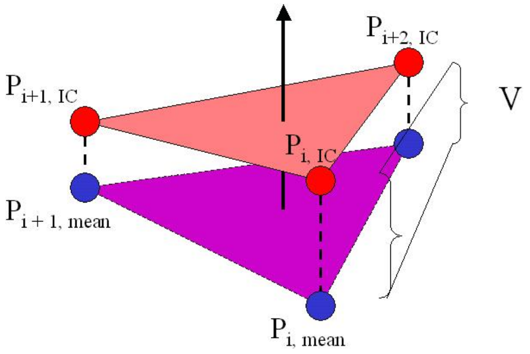

Figure 9.4: Illustration of the calculated volume between a triangle of the mean shape and a corresponding triangle of an estimated independent component.

Peaks with a peak value of over 50% of the maximum peak value are counted as peaks. The average volume of these peaks is taken as a measure of how the component has centered its shape changes in these few large peaks. Let n_{peaks} be the number of peaks, n_P the number of points included in these peaks, and V the volume of the significant peaks, then the measure L is defined as

$$L = \frac{V}{n_P n_{peaks}} \ . \tag{9.1}$$

Introducing this ordering measure, the independent components are estimated again, using the *FastICA* algorithm. This gives the independent components much more localized features as can be observed in Fig. 9.5(b) that has been colorcoded according to the shape variations. The principal components represent more global variations which can be observed in Fig. 9.5(a). These different characteristics can obviously also be observed in the value of the ordering measure.

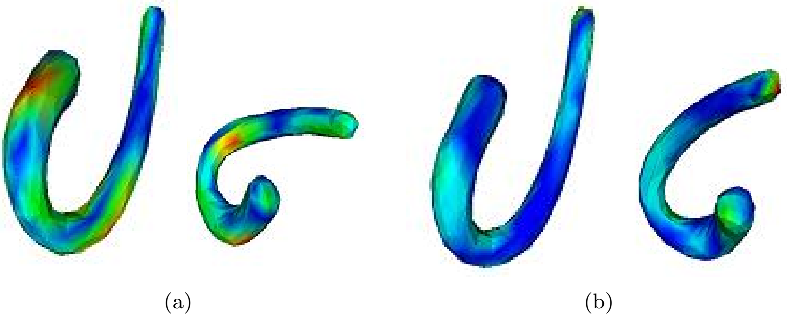
(a) (b)

Figure 9.5: Blue corresponds to no variation and red to maximum variation. (a) Aortic shape variations captured by a PCA mode. Notice the big variance in color over the whole aortic surface. (b) Aortic shape variations captured by an independent component. It is observed that the independent component show very localized features compared to the more global variations of the principal component.

It should be noted that the illustrated independent component is not well suited for separating normal subjects from patients, leading back to the issue that the distinction between the normal subjects and the patients is not very good. This issue is treated in section 9.3.

9.3 The Fisher discriminant

The hypothesis of this study is that connective tissue disorder is one of the sources shaping the aorta. The lack of an aparent ordering measure, having no exact knowledge of the distribution of the seeked component, it is modelled to be composed of two normal distributions. One is representing the normal subjects and the other the diseased subjects, offset by the difference between being diseased and having a normal aorta. The Fisher discriminant, evaluating the projection separation of the two populations, is expected to have its maximum at the true source and thus seems a well suited ordering measure. Initially canonical discriminant analysis was performed, as this method finds the optimum projection under the given assumption, but this did not yield a complete separation of the subjects.

The Fisher ordering measure has been implemented, and a resulting distribution is compared to the previously best obtained separation in Fig. 9.6. It is seen that the separation, using the Fisher ordering, is much better, though the groups are still not entirely separated.

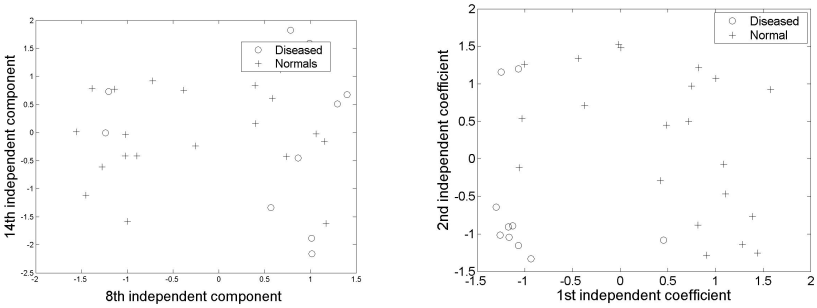

(a) (b)

Figure 9.6: Separation between normal (+) and diseased (o) subjects. (a) A typical best separation obtained with two of the features calculated using non-Gaussianity as independent component ordering. (b) Much better separating features using the Fisher discriminant as ordering measure.

Visual inspection of the independent components, shown in Fig. 9.7 yields that the coefficients corresponding to diseased subjects tend to have a dilation along the ascending aorta and the aortic arch. During the testing a rather strong dependency on the initialization was observed, giving inspiration to section 9.3.1.

9.3.1 Multiple Initializations

Due to the random initialization of the *FastICA* algorithm and multiple minima, it was also tried to initialize more independent components than could be estimated. The "best" components could then be selected by the ordering measure, and a complete separation could be obtained. This worked better when discarding the principal coefficients corresponding to the least significant variances. In Fig. 9.8 it can be observed that the groups can be separated linearly,

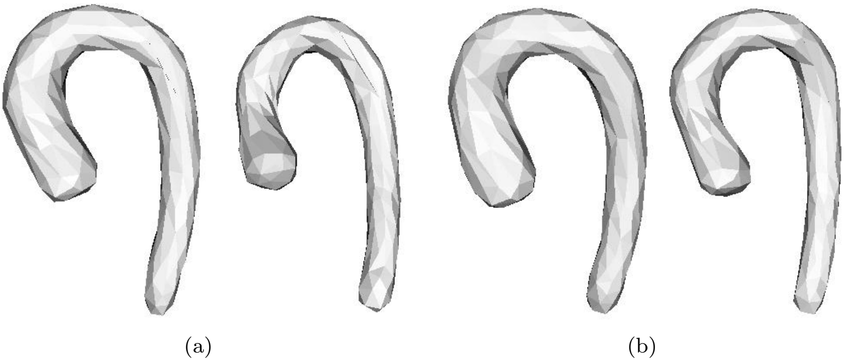
(a) (b)

Figure 9.7: Variation of the two best separating independent components, using the Fisher discriminant as an ordering measure for the independent components. Left corresponds to negative coefficients (diseased) right to positive coefficients (normals) (a) The first independent component, the diseased are seen to have a dilation at the ascending aorta. (b) The second independent component also with a dilation for the diseased subjects, apparently including a dilation around the beginning of the descending aorta.

though without a very clear division. Unfortunately the generalization is bad. The separation was best using around 14 principal coefficients, but this gives 13 degrees of freedom and only 31 samples, so we expect the problem to be that the solution is over-fitted to the presented data.

9.4 Conclusion

In this section it has been shown that using different ordering measures can improve vastly on the properties of the recovered components. Using a measure of localization has given very localized components and the Fisher discriminant as ordering measure showed a much better separation of the components. In section 9.1 it was learned that the number of free parameters was too high, giving components with no medical significance. This may also to some extent have been the case using the two other ordering measures.

Another problem with the two ordering measures is how to combine them. This and the poor ability to generalize is treated in chapter 10.

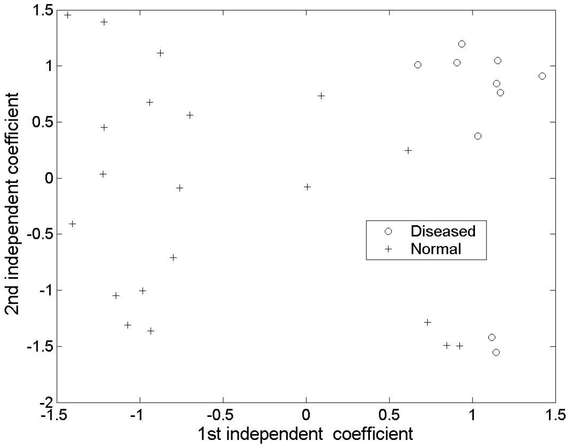

Figure 9.8: Distribution of the projections on each independent component, along the two first independent components. A linear separation is possible, though not very convincing.

Chapter 10

A novel approach to dimensionality reduction

In secion 9.3.1 it was reported that the generalization ability of the estimated independent components was very poor, and that this may be related to overfitting of the solution. This hypothesis has been investigated further, and a suggestion for a constraining scheme has been proposed, which is summarized in the article *Detection of Connective Tissue Disorders from 3D MR Images using Independent Component Analysis* that is to be orally presented at the Computer Vision Approaches to Medical Image Analysis (CVAMIA) workshop of the ECCV conference. The paper is appended in App. C. This section provides an elaboration of the reported work.

10.1 Sparse data

The number of dimensions is an important factor because the data is very sparse. The observed data, X, in this study has $d = n_{landmarks} \cdot 3 = 248 \cdot 3 = 744$ dimensions when using one phase and 1581 when using two phases of the cardiac cycle. The number of samples is still only 31, 21 normals and 10 diseased. As described in section 8.2, the data is projected onto the principal components. This is both out of computational convenience and because the data is only distributed along these directions. In section 9.3.1 it was reported that limiting the number of included principal components made an improvement to the separation of the independent components, but gave a poor generalization ability. This gives motivation to further reduce the number of free parameters in the estimation of the independent components.

10.1.1 The number of source signals

The data is describing the shape of the aorta and therefore the number of independent source signals is expected to be rather high. The physical shape of the subject, the gender of the subject, the height and the age of the subject could all be independent sources shaping the aorta. The one of interest in this study divides the subjects in two groups with versus without connective tissue disorders.

Due to the reduced number of free dimensions and the complex shaping of the aorta, there are probably more sources than dimensions of the observed signal (e.g. samples). This is in contrast to the original assumption behind the ICA model (8.1). Reformulating the model in the framework of the anlytically simple Kurtosis measure shows some interesting features, and is the topic of this section.

Maximizing the absolute value of the Kurtosis can be interpreted as recovering a projection that is only directed along a single of several independent components. Now examining $w^T X = w^T AS$, the common assumption in ICA is that $A_{d\times k}$ satisfies $d \geq k$ because in this way no constraints are imposed on z given by $z = wA$. This was also the assumption in section 8.3.1.1 where Kurtosis was introduced. Assuming that $d < k$ means that wA is only spanning a subspace of $\mathbb{R}^k$, the space of S. This could mean that some of the minima are not described in this subspace. Denote the subspace of R^k not spanned by wA by $\hat{V}_{k-d\times k}$. The additional constraints on z are given by (Eq. 10.1), where $0_{1\times k-d}$ is a vector of zeros due to the orthogonality.

$$z\hat{V}^T = 0_{1\times k-d} \tag{10.1}$$

The number of constraints under the maximization is bigger than the number of parameters and thus the earlier described minima can not be reached. The Kurtosis measure is still favoring distributing the z_i's on as few components as possible though. Meanwhile recovering a true independent component is not to be expected, the maximum will, by this objective function, be as independent from the other sources, as possible using a linear transformation.

10.1.2 Overcomplete source basis

Several locally stable projections are found by the *FastICA* algorithm. The outcome depends on the initialization of the algorithm, and it is assumed, based on the discussion in section 10.1.1 that the different projections favor different source signals. None of them may fully describe a true source signal, but it will be more or less represented in every projection. This is the motivation for choosing an ordering measure that favors the components that is believed to describe the desired sources well. An observation of section 9.3.1 was that the number of free parameters needs to be reduced. Based on the conclusion of section 10.1.1 that the ICA algorithms still favor few source signals in the presence of more source signals than observable signals, the idea of the current section is to constrain the estimation to include only a few observable variables at the time.

Let the total number of observables be denoted d and the number of independent sources k. In the specific case $d = 22$, retaining 97.5 % of the information and discarding the 8 least significant principal components. To reduce the number of degrees of freedom the search is constrained to only alter the coefficients corresponding to dividing the variance in $c = 5 \approx \sqrt{22}$ parts. This is illustrated by

$$X_d = A_{con} S_c \ , \tag{10.2}$$

where the constraints of the constrained matrix A_{con} are best illustrated by writing out the matrix representation.

$$\begin{pmatrix} x_1 \\ x_2 \\ \vdots \\ x_d \end{pmatrix} = \begin{pmatrix} a_{1,1} & a_{1,2} = 0 & \cdots & a_{1,c} = 0 \\ a_{2,1} & a_{2,2} = 0 & & a_{2,c} = 0 \\ \vdots & \vdots & & \vdots \\ a_{d_1,1} & a_{d_1,2} = 0 & \cdots & a_{d_1,c} = 0 \\ a_{d_1+1,1} = 0 & a_{d_1+1,2} & & a_{d_1+1,c} = 0 \\ \vdots & \vdots & & \vdots \\ a_{d_2,1} = 0 & a_{d_2,2} & \cdots & a_{d_2,c} = 0 \\ \vdots & \vdots & \ddots & \vdots \\ a_{d_{c-1}+1,1} = 0 & a_{d_{c-1}+1,2} = 0 & \cdots & a_{d_{c-1}+1,c} \\ a_{d_c,1} = 0 & a_{d_c,2} = 0 & \cdots & a_{d_c,c} \end{pmatrix} \begin{pmatrix} s_1 \\ s_2 \\ \vdots \\ s_c \end{pmatrix} ,$$

where the number of free parameters in each constrained independent component is $d_1 - 1, d_2 - d_1 - 1, ..., d_c - \sum_{i<c} d_i - 1$. In the specific case, the maximum is 6 free parameters (keeping in mind that all components are normalized to a unit length, taking one degree of freedom). To emphasize the calculation of one constrained independent component, the equation governing the ith component

under the above mentioned constraints is given by

$$x_i = \begin{pmatrix} x_{d_{i-1}+1} \\ x_{d_{i-1}+2} \\ \vdots \\ x_{d_i} \end{pmatrix} = \begin{pmatrix} a_{d_{i-1}+1,i} \\ a_{d_{i-1}+2,i} \\ \vdots \\ a_{d_i,i} \end{pmatrix} s_i \ ,$$

which can be estimated using the same algorithm as the usual ICA model (8.1).

The realizations in section 10.1.1 indicate that the estimated components found in (10.2) will not describe only one independent source. This observation, combined with the fact that prior information about the true source distribution exist inspires to allow a relaxation of the constraints given by (10.2) by including a second mixing matrix. Let the constrained mixing matrix be named A_{con} and the second mixing matrix $A_m(c \times c)$, then

$$X = A_{con} A_m S_c \ , \tag{10.3}$$

which gives a new model formulation for the estimation A_m

$$\tilde{X}_c = A_{con}^T X_d = A_m S_c \ , \tag{10.4}$$

since $A_{con}^T A_{con} = I_c$ due to the previous whitening of X. Equation (10.4) is seen to be of the same form as the ICA model (8.1) and the components can thus be estimated with the same method. The number of degrees of freedom in the model is observed to be reduced drastically.

The aortic shape of each subject is, after application of ICA, represented by the projection on the independent components. As the components are chosen with the property to divide the two populations, ICA is applied again on the most significant projections to extract more localized components using the same scheme as represented by (10.4). This is both due to a desire to obtain intuitively simple sources and because we a priori believe the sources are localized as discussed in section 9.2.

10.2 Example with more sources than observations

To illustrate the properties of maximizing the Kurtosis, an example of a randomly selected mixing matrix $A_{2\times 3}$ is chosen. This corresponds to 3 sources but only two observables. The Kurtosis of the three distributions are also randomly chosen by

$$\begin{aligned} A &= \begin{bmatrix} 0.6136 & 1.0320 & 0.7604 \\ -0.8242 & -0.4344 & 1.2546 \end{bmatrix} \\ K_1 &= 0.118 \quad K_2 = 0.7005 \quad K_3 = 2.133. \end{aligned} \tag{10.5}$$

The projection vector w is rotated from 0 to π and the size is set to match the constraint $\mathrm{E}\{(wX)^2\} = 1$. z is still defined by $z = wA$. The result is seen in Fig. 10.1. The rotation of w giving the maximum Kurtosis is seen to include mainly one of the three independent components, whereas the two eigenvectors, defined by the maximum and the minimum of the dash-dotted curve, are mixtures of comparable fractions of all three independent components. This illustrates the trend that the Kurtosis measure under constraints as without constraints is better than the PCA measure at isolating a few independent components.

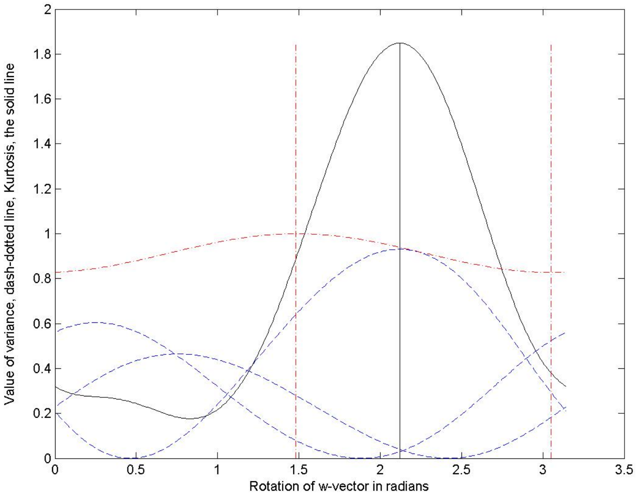

Figure 10.1: w-projections in an over-constrained independent component system. The x-axis is the rotation of w in radians. The solid line is the calculated Kurtosis with the maximum illustrated. The dashed lines are representing the fraction of variance contributed from each independent component. The dash-dotted line is the variance of the projection along the w-direction.

To investigate the matter further, and to affirm that the implemented *FastICA* algorithm gives the same result as the theoretical expectation, the sources and the mixing matrix is constructed with properties as described in (10.5). Sources with a specific Kurtosis can be constructed from a uniform distribution. A uniform distribution is described by the with and the density along the uniform part, the rest of the probability density is concentrated around zero, as illustrated in Fig. 10.2. The relation between the density and the width a is chosen so that the variance is one.

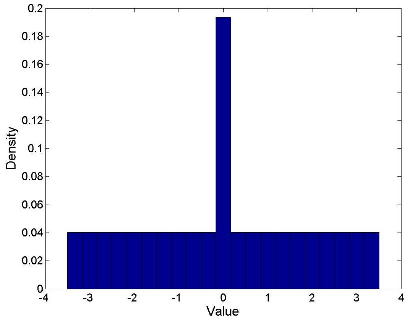

Figure 10.2: A uniform distribution with width $a = 3.34$ and density 0.0403, with the remaining probability concentrated around the value zero.

The Kurtosis of a distribution like the one illustrated in Fig. 10.2, with width a and density p can be estimated by

$$\begin{aligned}
\mathrm{E}\{x^2\} &= \int_{-a}^{a} px^2 dx = \frac{2pa^3}{3} = 1 \\
\Leftrightarrow p &= \frac{3}{2a^3} \\
\mathrm{E}\{X^4\} &= \int_{-a}^{a} px^2 dx = \frac{2pa^5}{5} = \frac{3a^2}{5} \\
\mathrm{kurt}(x) &= \frac{\mathrm{E}\{x^4\}}{(\mathrm{E}\{x^2\})^2} - 3 \\
\Leftrightarrow a &= \sqrt{\frac{5}{3}\mathrm{kurt}(x) + 3}\ , \qquad (10.6)
\end{aligned}$$

which means that deciding a value of Kurtosis, a distribution with the desired Kurtosis can be assigned by choosing the value of a and hereby also the value of p, as it is set to be of unit variance. Three such signals, with Kurtosis as described in (10.5), are illustrated in Fig. 10.3.

The three source signals are mixed with the mixing matrix from (10.5) to construct *two* mixtures, shown in Fig. 10.4.

A scatter plot of the two mixtures is seen in Fig. 10.5. It is observed that the high density around zero for all the distributions results in three lines in

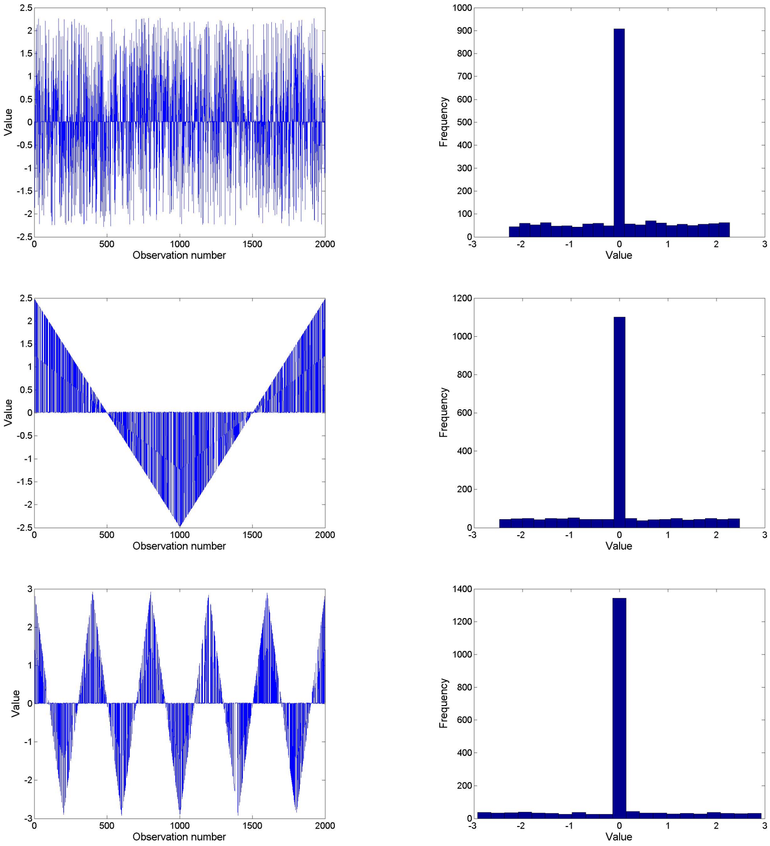

(a) (b)

Figure 10.3: Three source signals, with Kurtosis of 0.118, 0.7005, and 2.133. (a) The constructed signals. Most of the values are set to a small random number. (b) The resulting histograms. All have approximately unit variance and zero mean.

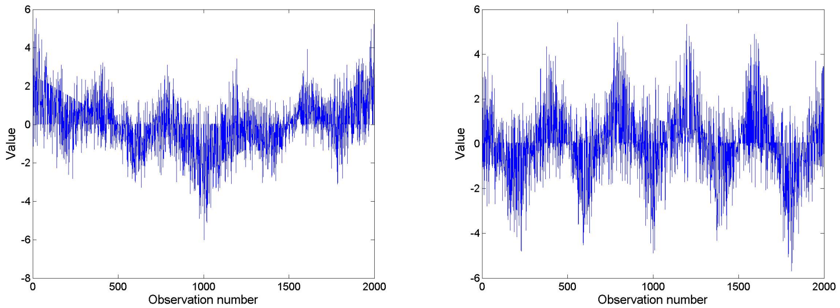

Figure 10.4: The two signal mixtures. It is possible to spot all the three independent sources in the mixtures, but hard to make out, how to separate them.

the scatter plot. The density is by far the highest in the center of the plot, corresponding to all three sources assuming small values.

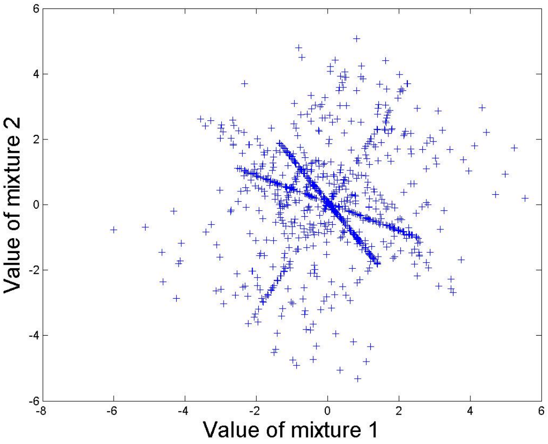

Figure 10.5: A scatter plot o the two signal mixtures. The three independent sources can best be identified by their high density around zero.

The *FastICA* algorithm was applied on the two mixtures to assess if the algorithm gives results similar to those expected by the Kurtosis analysis in Fig. 10.1, where a clear maximum of the Kurtosis is seen where the projection mainly consists of one independent source, namely the third one, with the highest Kurtosis value. The other component will, due to the whitening, be orthogonal to this component, and will thus include almost none of this component, but a mixture of the two other components. The resulting estimated sources of the *FastICA* algorithm is illustrated in Fig. 10.6(a), and a clear correspondence between the third independent source, seen in Fig. 10.3, and the first estimated independent signal can be seen. The second component can clearly be seen to be a combination of the two other sources as is expected by the previous analysis on Kurtosis.

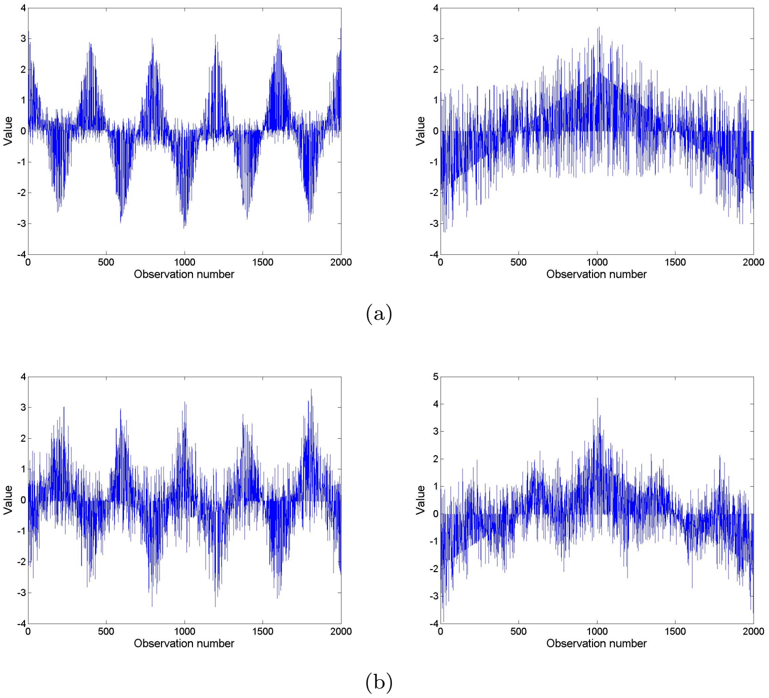

(a)

(b)

Figure 10.6: (a) The demixed signals, obtained using the *FastICA* algorithm. (b) The principal coefficient are clearly mixtures of all sources to a higher extent than the independent components.

Comparing the estimated independent components with the principal components shown in Fig. 10.6(b), it is evident that the independent components describe the sources more precisely. Whereas the principal components both seem like mixtures of all components the independent components appear like either a mixture of the two sources or a single sources with only a little of the random source added.

To investigate the matter further, the scatter plots of the projections are examined in Fig. 10.7. Note that the different sources are distributed along the dense lines that are visible in the scatter plot, because for all distributions the values around zero are the most frequent ones. The longer line correspond to the third independent source having the largest Kurtosis. In Fig. 10.7(a), showing the two independent components, it can be seen that this line is almost exactly aligned with the first independent component. The second component is a combination of the two other components as can be seen by the orientation of the these lines. In Fig. 10.7(b) the distribution of the principal coefficients is illustrated, and there is clearly not much tendency in any of the principal components.

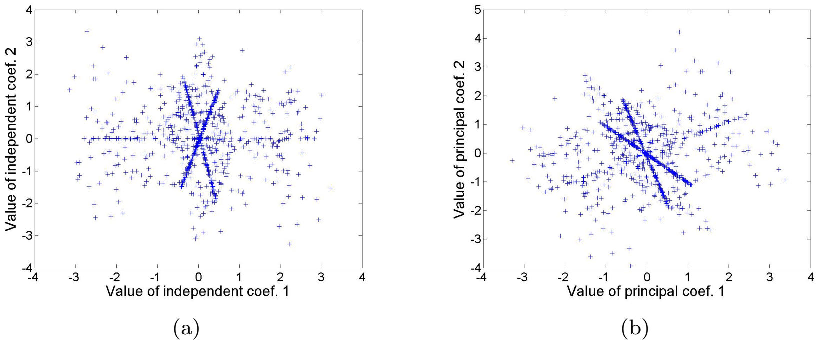

(a) (b)

Figure 10.7: Scatter plots where the direction of the different sources is appearent through the lines with higher density. (a) The independent coefficients. (b) The principal coefficients.

To summarize this illustration of independent component analysis in the presence of more sources than observables, it can be concluded that ICA was a better tool for extracting the sources than principal components.

Chapter 11

Time-invariant ICA model

The modification of the ICA model presented in chapter 10 proved to create a more robust estimation of the independent components working on only a single phase. Increasing the number of phases in the analysis did not improve the classification accuracy. The extra phases are included in the calculated principal components and do effect the principal coefficients forming the basis for the independent component analysis, but there seems to be a tendency that capturing the desired variations becomes harder, when the dimensionality of the problem increases. This was the motivation for developing a new model including time-invariant independent components. The basic assumption is that some time-invariant components exist along with some time-variant components. The work has been reported in a paper submitted to the MICCAI'06 conference, awaiting review, available in App. D. The current section is an attemp to elaborate the description of the idea presented in the paper. For the presented model the landmarking scheme had to be altered to consist of *time corresponding landmarks*, meaning to say that the landmarks in different phases were assigned using the same template.

11.1 Time-Invariant ICA

The time-corresponding landmarks consist of 243 three-dimensional points. It is assumed that the independent sources explaining the shape-variation can be divided in time-variant and time-invariant sources. The ICA model can be formulated as

$$X_{729\times 1}(t) = A_c s_c + A_t(t) s_t = [A_c \quad A_t(t)] \begin{bmatrix} S_c \\ S_t \end{bmatrix} , \tag{11.1}$$

where A_c represents the time-invariant components and S_c the corresponding time-invariant sources. $A_t(t)$ are the time-variant components with corresponding time-independent sources S_t. All 16 phases of the cardiac cycle can now be represented by the following model

$$X_{729\times 16} = [x(1)\ x(2)\ \cdots x(16)] = [A_c\ A_t(1)\ \cdots\ A_t(16)] \begin{bmatrix} S_c & S_c & \dots & S_c \\ S_t & 0 & \dots & 0 \\ 0 & S_t & \dots & 0 \\ \vdots & & \ddots & \vdots \\ 0 & 0 & \dots & S_t \end{bmatrix} ,$$

where $X_{729\times 16}$ is the concatenation of all the 16 aortic phase instances of a subject. It is assumed that a time-invariant source exists, only related to the disease status of the subject. The source represents the same shape variation independently on the phase of the heart cycle. This is an important assumption, since 16 instances exist of each of the 31 subjects, augmenting the total number of aortic instances to 496 for the estimation of the independent components. The model given by (11.1), along with the usual ICA implementation, is used to determine the time-invariant components. The different phases are correlated in their variation to some degree, but this model is still expected to be more robust than the one-phase model.

The independent component related to connective tissue disorders is most likely time-variant to some extent. The flow of blood and the aortic motion are both affecting the shape during the cardiac cycle. However, the component was divided in a time-invariant and a time-variant component. The time-invariant part can be estimated using far more instances of the aorta resulting in a more robust classification. Only one source related to being diseased is expected to exist, but as discussed in chapter 10, we expect the recovered components to be combinations of several true independent components. Therefore it is relevant to include more than one component in the later classification. The time-variant part of the component is estimated phase-wise based on the 31 instances of a specific phase of the aorta.

CHAPTER 12

The diagnostic step

Finding a single independent component distinguishing between diseased and normal subjects has not proven possible. This is discussed more thoroughly in chapter 17 but to summarize; more than one component may be needed to describe all connective disorders. The Fisher discriminant was introduced as an ordering measure in section 9.3 and may help to assess if a component contains valuable information in the diagnostic step. The choice of classifiers is explained in section 12.1, the quadratic classifier is the topic of section 12.2, and the perceptron classifier is explained in section 12.3.

12.1 Choosing a classifier

Concentrating on the components seemingly containing the most discriminative information about the two groups, a classifier is still needed to make the diagnosis decision. Important aspects in choosing a suitable classifier are

- The number of features.
- The complexity of the classification task.
- The complexity of the classifier.

- Intuitive intepretation of the classifier output.

The number of interesting features can be reduced to only two or three, using the Fisher discriminant and multiple initializations is to obtain a few diagnostic-wise interesting components. The classification task is rather simple once good independent components have been selected. Since the number of samples is very small (only 31 subjects available), there appears not to be sufficient evidence for creating a very complex decision boundary. This, in terms, means the classifier preferably should be rather simple. Because the final diagnosis will be given by a physician, it is important that he can validate that the decision is based on a sound foundation. Visual inspection of the decision rule is considered as a rather strong argument. A cuadratic classifier has most of the desirable properties and was the basis of the classification step in the work described in chapter 10. The perceptron classifier furthermore has a linear decision boundary where the normal vector can be illustrated visually. This could be presented alongside the actual instance of the aortic shape, to affirm that the caught variation is indeed present in the shape.

12.2 The quadratic classifier

The quadratic classifier is very well described in the litterature and the decision rule will just be emphasized here along with the assumptions made [36]. The prior probabilities are assumed equal, knowing that this probably gives a small bias to classify subjects as diseased, as the apriori probabilities seem hard to estimate. The quadratic discriminant function is given by

$$g_i(X) = -\frac{1}{2}X^T\Sigma_i^{-1}X + \mu_i^T\Sigma_i^{-1}X - \frac{1}{2}\mu^T\Sigma_i^{-1}\mu - \frac{1}{2}\log|\Sigma_i| \ , \qquad (12.1)$$

where Σ_i and μ_i are the estimated covariance matrix and mean for the two distributions.

12.3 The perceptron classifier

The implemented perceptron classifier is adapted from [37] getting a bit of inspiration from the support vector machine, which tries to maximize the distance between two groups.

The perceptron searches for a projection vector a_{d+1} including a bias that separates the populations, letting the sign decide how to classify a sample. Samples that are misclassified are collected and added to the projection vector. To find a better separation, a constraint is put on the distance to zero, so the distance from the separating hyperplane to all the points can be maximized for increased generalization ability.

Chapter 13

Implementation

The algorithms and preprocessing of the data have been implemented in *Visual C++ 6.0*. Some of the graphs presented in the current report are generated using *MATLAB 6.5*. This section is intended to give an overview of the implemented code, organized as a short description of the different implemented classes.

The different implemented classes are listed in Fig. 13.1. Direct dependency is illustrated with an arrow.

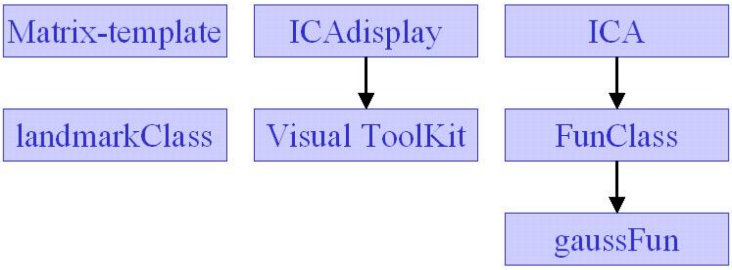

Figure 13.1: List of implemented classes, strong dependencies are listed with an arrow.

The different classes together form the backbone of all the analysis performed as described in this chapter. The following is an attempt to give some insight into the structure of the implemented program.

- **Matrix-template** A matrix-template was developed using core features like principal component analysis and matrix inversion from an existing array class made by Steve Mitchell. This new matrix class is a template class, meaning it can be defined for all variable types, and uses operator overloading, allowing pseudo-normal syntax in matrix calculations, very much similar to the syntax of *MATLAB*. This matrix-template is applied by all the implemented classes and functions, and serves as a format for exchange of data between classes.

- **landmarkClass** As the landmarked data had its origin from several sources and was stored in different formats a general procedure was build into the *landmarkClass*. It also reads and stores the triangulation of the shape, if a such exists.

- **Visual Toolkit** A toolkit developed open source by *Kitware* which can be downloaded free of charge. It is a rather powerfull toolkit for visualization, but has proved hard to learn being new to the concept. Two books exist on the toolkit, which have shown to be very useful [38] [39].

- **displayICA** A function has been created to display the variety of ICA results in different ways, as illustrated in the current report. This function is based on the Visual Toolkit.

- **ICAclass** A class that contains the implementation of the different algorithms implemented in this work. To keep the implementation general, the functions are implemented as a *FunClass* that for instance has its functions overloaded by $-\exp^{-\frac{-x^2}{2}}$, named *gaussFun* in the case of the negentropy approximation for the *FastICA* algorithm.

Part III

RESULTS

Outline of the presented results

The objective of the presented study was three-fold. A partial objective was to obtain a good automatic segmentation of the aorta. This was obtained previously, but the results are provided in chapter 14 for completeness, as they form the basis of the current work. The reported methods are briefly reviewed in chapter 6. A second goal was to obtain features describing the aortic morphology, which is presented as the independent components in capter 15, both in the single-phase situation, and the time-invariant features extracted from the 16 phases of the cardiac cycle. The diagnosis step based on the estimated independent components is validated in chapter 16 applying a leave-one-out test on the data.

Chapter 14

Segmentation results

The developed segmentation method produced aortic surfaces with subvoxel accuracy as judged by the signed surface positioning errors of -0.09±1.21 voxel (-0.15±2.11 mm) and unsigned positioning errors of 0.93 ± 0.76 voxel (1.62± 1.25 mm). An example of a typical segmentation result is shown in Fig. 14.1. The segmentation result is shown in transverse and coronal views. For each view shown in the figure, 4 slices were randomly selected from the 3D image. The volumetric representation of segmentation is shown in Fig. 14.2. Fig. 14.3 summarizes the signed positioning errors obtained for each image.

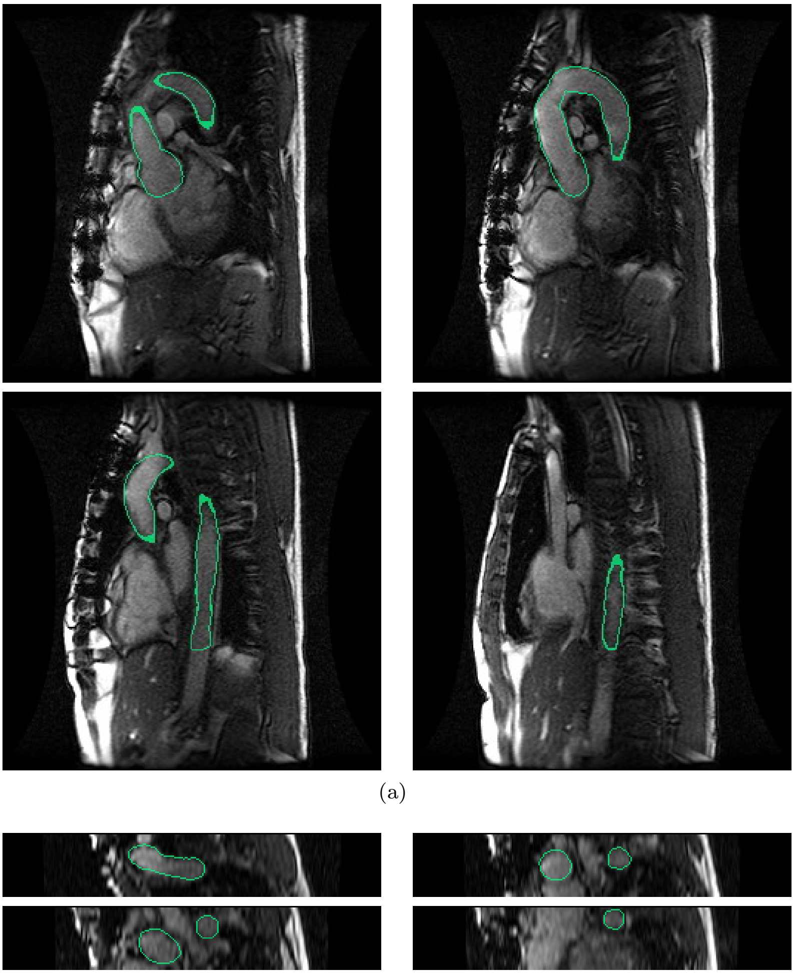

(a)

(b)

Figure 14.1: Automated segmentation result in 4 randomly selected slices; the segmentation outlines are shown in green. (a) Transverse view. (b) Coronal view.

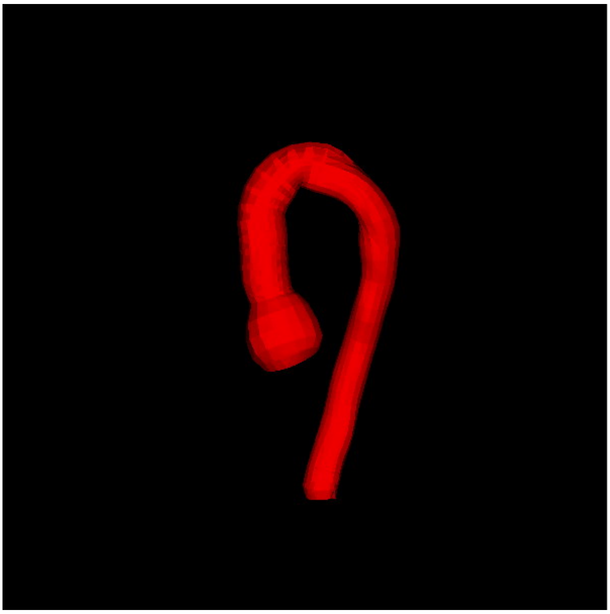

Figure 14.2: Volumetric representation of the segmentation result.

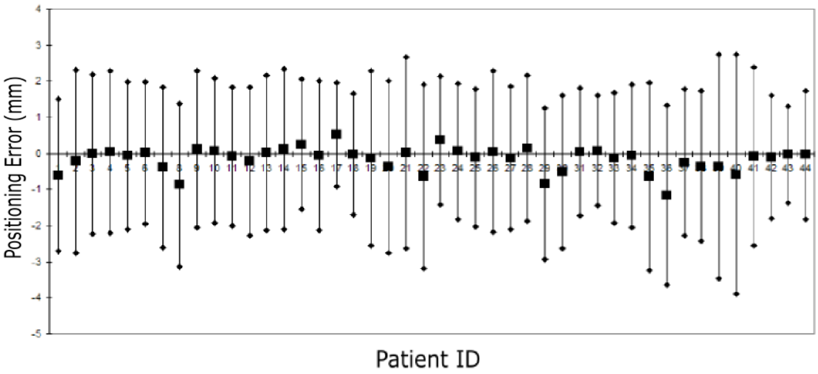

Figure 14.3: The average signed positioning errors for all analyzed images.

Chapter 15

ICA Results

The ICA results are divided in the analysis of a single phase from the 31 available subjects and the estimation of time-independent components from all 16 phases of the cardiac cycle.

15.1 Single-phase ICA results

Fig. 15.1 illustrates the shape variations captured by the first and second independent components on the first phase. The analysis suggests that the first independent component represents the variation in the length at both ends and to a smaller extent the shape of the aortic arch. The second independent component shows less localized variations concentrated along the ascending aorta. None of the components seem to have much effect on the descending aorta, which corresponds well to the clinical expectation stating the effect is centered around the arch, as described in section 3.

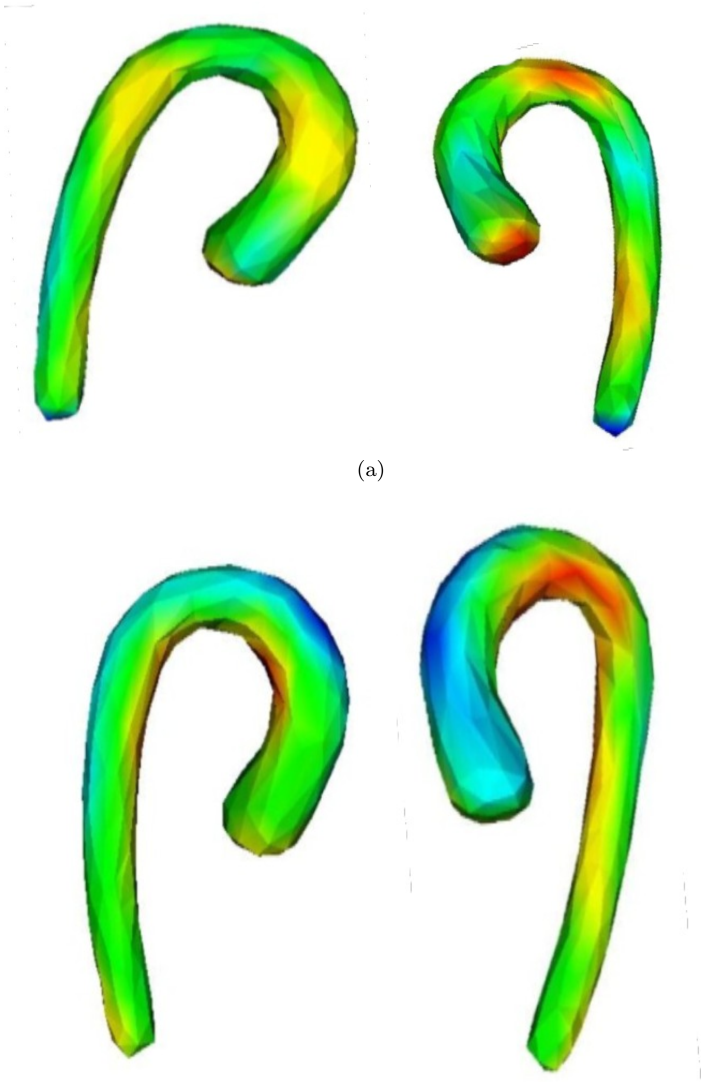

(a)

(b)

Figure 15.1: Aortic shape variations observed in the analyzed population. Red corresponds to negative variation, compared to the normal of the mean-aorta, on which the variances are projected. Blue corresponds to positive variation. Positive values of the projection correspond to a higher likelihood of having a connective tissue disorder. (a) Shape variations for the first independent component on both sides of the aorta. The aortic shape corresponding to a diseased subject is seen to have a "flatter" and slightly dilated aortic arch. (b) Shape variations for the second component, again from both sides. The diseased subjects corresponding to the positive blue is seen to have a more rounded arch, and a dilation around the ascending aorta.

15.2 16 phase ICA results

The two first time-invariant independent components estimated using all 16 phases are illustrated in Fig. 15.2. They both describe diseased subjects with thicker ascending aorta and the first one also a thicker aortic arch and start of the descending aorta. This also corresponds the clinical observations of connective tissue disorder, though the components are less localized, which indicates variation in between phases.

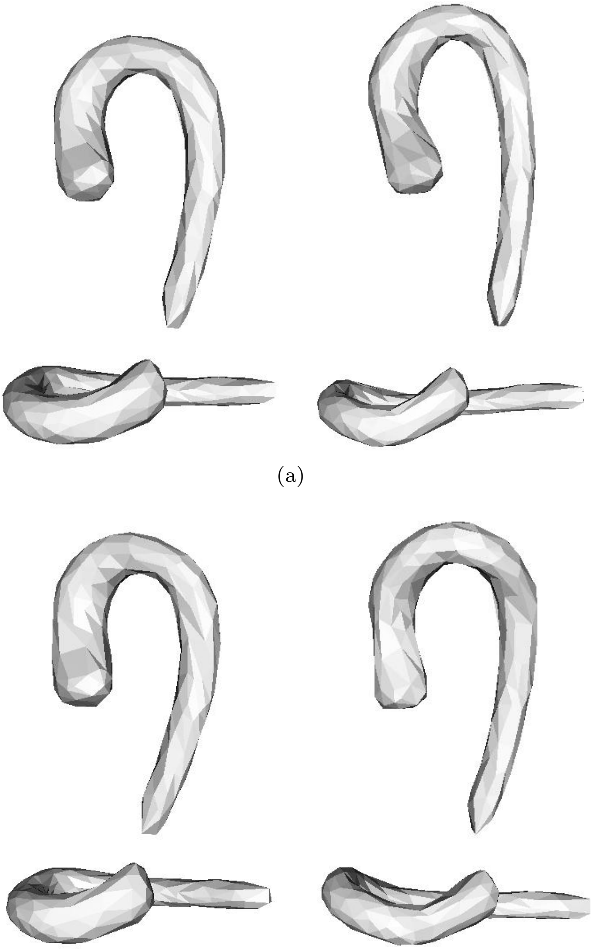

(a)

(b)

Figure 15.2: Aortic shape variations described by the first two time-invariant independent components, shown as the mean shape ±2 standard deviation. (a) The first time-invariant independent component. It can be observed that the diseased subjects (left) seem to have a thicker arch and in particular a thicker ascending aorta. (b) The second component. The diseased subjects (left) also appear to have a thicker ascending aorta and a flatter aortic arch.

Chapter 16

Diagnosis Results

The diagnosis results can be divided in the results obtainable considering only a single aortic phase or the same model applied on two phases, and the obtained results utilizing the extra information in all the 16 phases.

16.1 Single-phase and two-phase results

The distribution of the projection of the data on the two first independent components, shown in Fig. 16.1, illustrates that the separation task can very well be performed by a simple classifier. The evaluation is done using a leave-one-out approach and though it always appears possible to find independent components dividing the two populations, it is not guaranteed to generalize to the unseen sample.

For the single-phase case, 248 landmarks were automatically generated on each aortic luminal surface. The quadratic classifier working on two independent components exhibited a sensitivity of 80%, meaning that 80% of diseased were diagnosed as such and a specificity of 100%, meaning that all normal subjects are classified as being normal in the leave-one-out test. When working on two phases, 248 landmarks on the first phase of the aortic surface and 279 landmarks

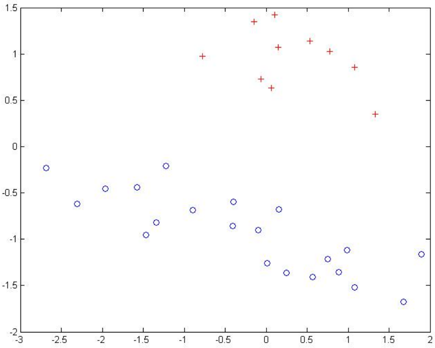

Figure 16.1: Projection of data along the two first independent components. Diseased subjects are marked with '+' and healthy subjects with 'o'. A clear separation is observed.

on the aortic surface in the middle phase were included. The classification proved worse, namely a sensitivity of only 70% but still a specificity of 100%. The analysis on two phases using the same model was performed to compare the method to the previous work using a support vector machine, reported in [2]. The localization ordering measure was designed for only one object and not two phases and this may have affected the outcome.

The overall results are summarized in table 16.1 and table 16.2, showing the confusion tables of the single-phase model and the two-phase model.

The single-phase model applied to either one of the two phases gives the same confusion table, but one of the errors in classifying the diseased was for different subjects, so a combination of the one phase models, believing that the specificity is really 100% would actually give an even better classification. The very encouraging results obtained analyzing a single phase work well as a motivation for further exploration analyzing 2 phases and all available 16 phases. Initially the constraints on the ICA were a simple constraint as described earlier setting the elements corresponding to the last 16 principal components to zero. This gave a good separation, but the limited ability to generalize lead to less than perfect specificity and only 40% sensitivity. An issue that might make the sensitivity worse than the specificity is that the number of diseased is only 10 compared to 21 normals. As only two independent components were needed for the classification task, it seems that when using prior knowledge of desired features of the component, more task-specific information can be contained in the independent components than in the higher-variance principal components. The previously implemented support vector machine needed 9 principal components.

	Predicted	
Disease Status	Diseased	Normal
Diseased	8	2
Normal	0	21

Table 16.1: Classification results of the single-phase model

	Predicted	
Disease Status	Diseased	Normal
Diseased	7	3
Normal	0	21

Table 16.2: Classification results of the two-phase model.

16.2 16 phase results

Fig. 16.2 shows the distribution of the projections of the 16 phases of the different subjects. The diseased subjects tend to have negative values of both components. The dilation of the components is located differently for the two components and it is seen that the different aortic instances are combinations of the two, each corresponding to a different position of the aortic dilation.

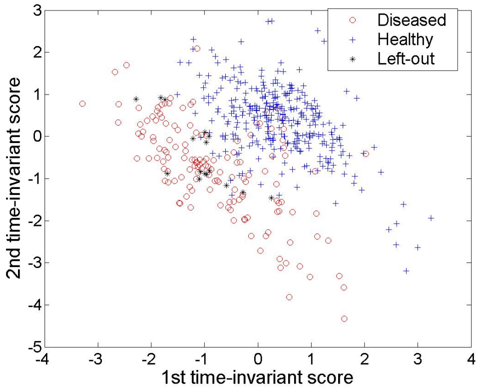

Figure 16.2: Projection of data along the first two time-invariant independent components. The arotic instances of the left-out diseased subject are seen to be distributed among the other diseased subjects.

The projections along the time-variant and time-invariant independent components were combined using a perceptron classifier on each phase. In the last classification step the phases 1, 7 and 8 were included, corresponding to the phases around the cardiac R-wave peak and in the middle of the R-R interval. This gave more robust results. Results of a leave-one-out test can be seen in Table 16.3. Only one diseased subject was wrongly classified as being normal.

This is an improvement from the one-phase results that classified two diseased subjects as normals. The advantage of the reported ICA-method is the ability to verify that the features it captures, correspond to the clinical expectation, namely dilations around the aortic arch, and the ascending aorta.

	Predicted	
Disease Status	Diseased	Normal
Diseased	9	1
Normal	0	21

Table 16.3: Leave-one-out classification results of the 16-phase model

To assess the classification in more details Fig. 16.3 has been generated. From this we can learn that one of the diseased subjects appears more healthy than one of the healthy subjects, but only, when the diseased one has been left out of the independent component estimation.

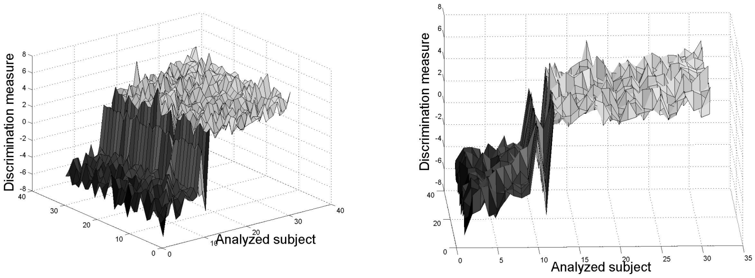

Figure 16.3: A confusion matrix of the results of the leave-one-out test. It can be observed that the values are generally a bit closer to the decision boundary, zero, in the diagonal, where they have been left out of the independent component estimation. NB. ”out subject” refers to the left-out-subject.

Part IV

Discussion and conclusion

CHAPTER 17

Discussion

The results described in chapter III are good however, there is still room for improvement. In every aspect, we are interested in getting as precise descriptors, as possible, for the diagnosis. Some weaknesses of the proposed models have been considered and are summarized and some ideas for further investigation are described. It should be emphasized that it is a list of apparent problems rather than a *complete* list of possible problems.

- **The independent component assumption**

  It is doubtful whether *one* independent component can explain all the possible variations observed in subjects with connective tissue disorders. Suppose that several components are needed (as for the practical diagnosis task), then they should describe different independent connective tissue disorders. Otherwise, if they were describing the same phenomenon, they would obviously be inter-dependent, and the basic independency assumption (8.1) of the analysis would not be met. The two components shown in Fig. 15.1 each show distinct characteristics, but this may be a consequence of the described estimation method. With the limited number of subjects it appears difficult to conclude anything statistically significant on this issue.

- **Analysis of variation**

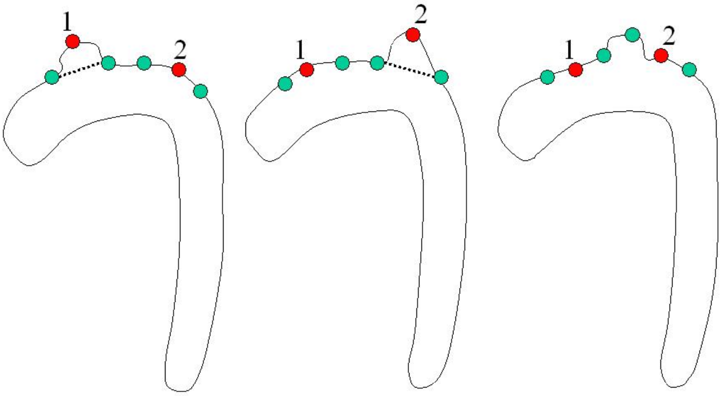

Figure 17.1: Demonstration of how features 1 and 2 that are present in the ”training data” (the two left figures), is not present in the rightmost figure, even though it clearly has a similar dilation.

Suppose a situation like the one depicted in Fig. 17.1 existed. To a human observer, it is apparent that the third example is of the same kind as the two presented examples, assuming the two first belong to the same class of illness. This will not be captured by the independent component analysis, as it only can capture variations that globally resemble a presented case, even though the local correspondence is very much alike. This means that a given local variation has to be present at the same global position, to be recognized.

- **Landmark dependency**

  The model captures variations by doing statistics on the chosen landmarks. The result is that every variation in the precise landmark assignment, will also have an effect on the statistical analysis. Possibly this could be avoided by considering landmark-free shape models. Since it has been observed that the descending aorta has little or no significance as a classification feature, it might also be an idea to discard it from the analysis all together, to avoid chance correlations. A different approach could be a thinning of the correlation over distances, which could be another way to reduce chance correlations.

- **Sparse data**

  The major issue of the current work has been the very limited amount of available data. The acquisition of data is work intensive and expensive. In time more data will be available for the study, but the number of subjects will still be limited. The considerations on sparse data preseneted in chapter 10 are valid in many medical applications that mostly suffer from the same problem.

Related to the correlation thinning discussed previously, it is interesting if the goal of obtaining localized independent components is achievable. Suppose an independent component has been estimated, depending only on variations in a small localized area of the aorta (maybe even of *one phase* only). The analysis then has isolated the variation in this area, independently of the configuration of the rest of the aortic shape. To make this observation that all other variations occur independently of this local variation, a significant number of samples would be required.

A different approach to the problem of an insufficient number of samples might be to make a ”rotation” and consider the subjects as observations and the landmarks as samples. This would augment the number of ”samples” to several thousands. A parallel to this approach is an efficient way of calculating a singular value decomposition, however it has not been investigated further, as the independence condition between sources is not always expected to hold true, which is illustrated in Fig. 17.2. The current implemented methods do also include some assumptions that may only be partially met, so it could still make sense to engage in further investigations of this idea.

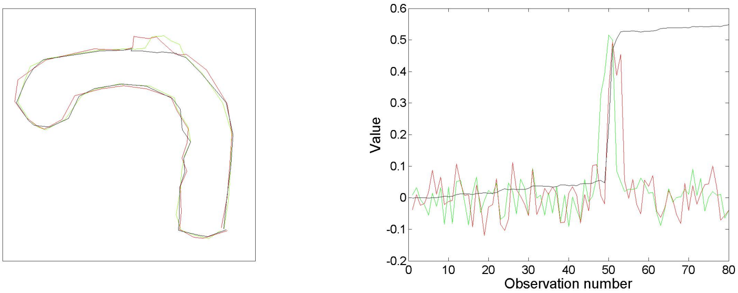

(a) (b)

Figure 17.2: Examples of two independent sources. (a) The two shapes are colored green and red, and the mean shape is black. It is seen that they have an overlap in common. (b) The value of the observations, subtracted the mean shape. Still one shape is represented by green and the other by red. The black curve illustrates the cumulative estimated covariance of the components, which are seen not to be independent.

Yet another approach could have been to use the orthomax, varimax or sparse principal component analysis (SPCA) algorithms instead of the ICA, but they unfortunately lack the generative model of the analyzed data, which gives a more physical interpretation of the components. Conversely it could be argued that the very small number of samples means that investigating the distribution in multiple dimensions, is not optimal for a general analysis.

- **Structure of the components**

  It is observed that the components have quite a bit of structure. Methods for independent component analysis on signals with a time structure have been developed, making separation by either autocovariances or by changes in the variance of the signal [31]. This can not immediately be applied to the artic shape, as it is a surface distributed in two dimensions, and not just in one dimension as a time-signal. But creating a two-dimensional reference system on the aortic surface, it could prove an interesting way to exstract components.

The presented considerations consist of some the possible problems and suggestions to their solutions, but not necessarily all problems, as the problem was indeed a very complicated one.

CHAPTER 18

Conclusion

Early detection of connective tissue disorders leading to aortic aneurysms and dissections is potentially an important tool in a prophylactic treatment of these severe diseases. Objective identification of subjects with connective tissue disorders is shown to be possible from 4D aortic MR images. Automated and accurate segmentation of the aorta in 4D (3D + time) MR image data is reviewed, and a computer-aided diagnosis (CAD) method using independent component analysis (ICA) is reported.

The presented problem is ill-posed, with a high number of dimensions compared to the number of samples (subjects), but the developed ICA model was a suitable approach for capturing the structural shape variations important to the classification task.

Two different ordering measures have been introduced, based on conclusions drawn from the performed analysis. Except for being generally applicable ordering measures, they also demonstrate that the ICA results can be vastly improved by choosing an appropiate ordering of the independent components. In many cases would probably be useful to model the desired sources, and order the corresponding independent components accordingly.

To improve on the generalization ability, a method for constraining the estimation of the independent components was developed. This constraining method may very well be applicable in other medical imaging challenges, as the problem of sparse data is very common in the medical imaging field. A paper presenting the method (App. C) and the obtained results, has been accepted for oral presentation at the CVAMIA'06.

The concept of time-invariant independent components has been introduced, and it has been shown to have great use in the extraction of the information from several available phases in the classification step. In many applications, data is available from several time steps, and this could be a way to extract information from it. Especially when data is sparse it may help to increase the robustness of the feature extraction, as has been demonstrated in the current work.

4D MR image data sets acquired from 21 normal and 10 diseased subjects were used to evaluate the efficiency of the methods. The obtained ICA results have been validated by performing a leave-one-out classification task on the most significant features, as well as performing a visual inspection of the components. A quadratic classifier and a linear perceptron classifier were both sufficent for the classification task, and when using a single phase of the cardiac cycle, 8 out of 10 diseased subjects were identified and the specificity was 100 %, classifying all 21 healthy subjects correctly. With 4D information included in the analysis by using the estimated time-invariant components, the developed CAD method classified 9 out of 10 diseased correctly, and still the specificity was 100 %. The independent components were inspected visually to further substantiate their validity, and this analysis showed good correspondence between the clinical observations and the estimated indendent components.

Part V

Appendix

Appendix A

Aorta examples

The aortic shape of 10 diseased subjects and 10 normal subjects are illustrated for the first phase in this appendix.

Subject reference list	
Diseased subjects	Normal subjects
p99308931-030612-1226	p01487814-041019-1457
p98088726-020826-1138	p32871631-040818-1043
p96947008-030214-1046	p70083176-040803-1147
p89311241-030923-1129	p87159991-041119-1550
p88249033-021204-1548	p95094481-041018-1332
p77188991-030502-1606	p98013520-041115-1539
p76043978-040716-1011	p98013891-041116-1539
p75047514-040319-1339	p98374221-040929-1455
p72151835-020118-1418	p99402301-040928-1506
p01005182-040216-1315	p99540886-041215-1541

Table A.1: List of illustrated subjects

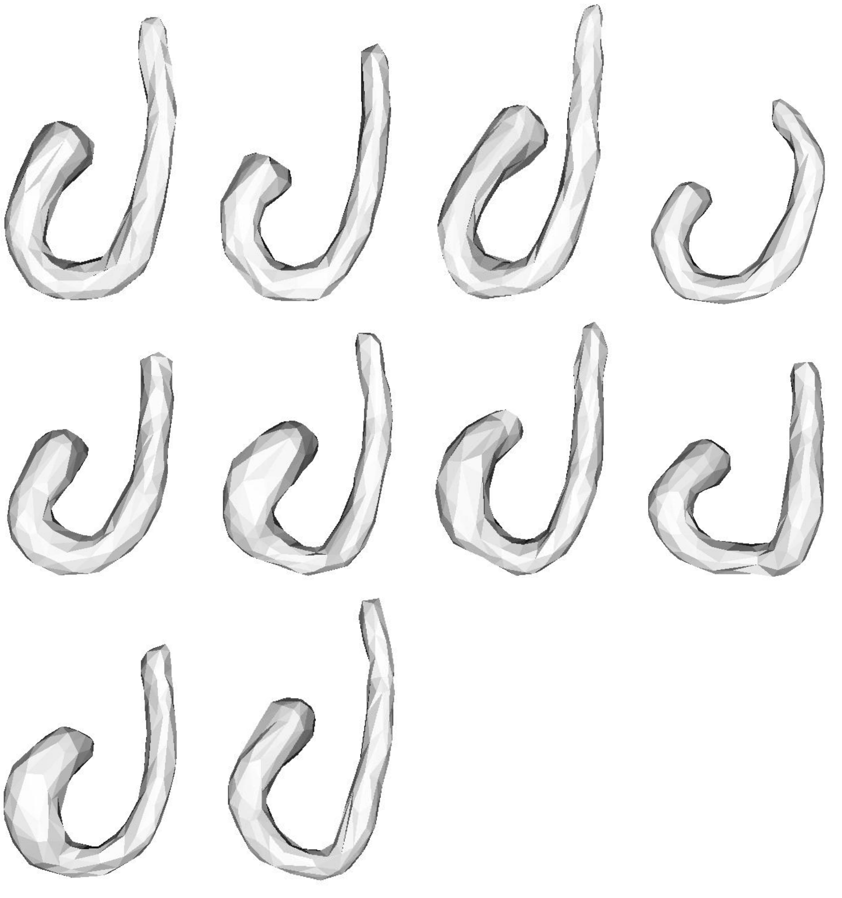

Figure A.1: Diseased subjects.

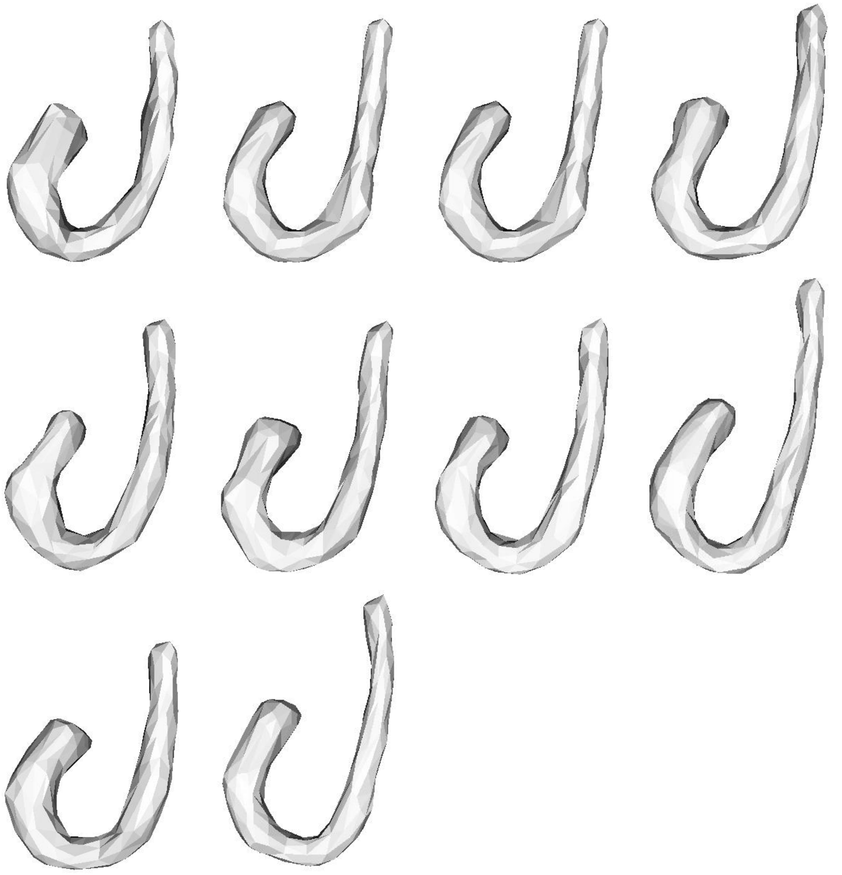

Figure A.2: Normal subjects.

APPENDIX B

The fastICA algorithm

In this section the fixed-point *fastICA* algorithm is developed using negentropy. The *fastICA* algorithm is a fixed-point algorithm, which means that when it converges like

$$w = f(w) \ . \tag{B.1}$$

Let $\mathrm{E}\{G(wX)\}$ be an approximation of the negentropy then

$$\nabla_w \mathrm{E}\{G(wX)\} = \mathrm{E}\{Xg(wX)\} \ , \tag{B.2}$$

where $g(wX)$ is the derivate of the approximation $G(wX)$. Now inspired by the gradient descent algorithm, the fixed-point algorithm is constructed so the weight vector is aligned with the gradient. This can be modified a bit, and we get

$$\begin{aligned} w &= \mathrm{E}\{Xg(wX)\} && \text{(B.3)} \\ (1+\alpha)w &= \mathrm{E}\{Xg(wX)\} + \alpha w \ , && \text{(B.4)} \end{aligned}$$

where (B.3) still holds true for all values of α. This is recognized as being very similar to the Lagrange condition, when optimizing $\mathrm{E}\{G(wX)\}$ under the constraint that $\|w\|^2 = 1$, which gives

$$\mathrm{E}\{Xg(wX)\} + \beta w = 0 \ . \tag{B.5}$$

Let F be the left-hand side, then

$$\frac{\delta F}{\delta w} = \mathrm{E}\{XX^T g'(wX)\} + \beta I \ . \tag{B.6}$$

This can be approximated by noting that X is sphered, to get $\mathrm{E}\{XX^T g'(wX)\} \approx \mathrm{E}\{XX^T\}\mathrm{E}\{g'(wX)\} = \mathrm{E}\{g'(wX)\}I$. Thus according to the newton iteration

$$\begin{aligned} w(n+1) &= w(n) - [\mathrm{E}\{Xg(wX)\} + \beta w]/[\mathrm{E}\{g'(wX)\} + \beta] \\ \Rightarrow w(n+1) &= \mathrm{E}\{Xg(wX)\} - \mathrm{E}\{g'(wX)\}w \ , \end{aligned} \tag{B.7}$$

remembering that the $w(n+1)$ is normalized in every step, and that the sign is also arbitrary.

This completes the fixed-point iterations in the *fastICA* algorithm. A typical approximation $G(wX)$ to the negentropy is the function $G(x) = -\mathrm{e}^{-x^2}$, which has also been implemented in the current report. The developed fixed point algorithm converges towards independent components, which was proved by Hyvärinen et al. [31].

Appendix C

Detection of Connective Tissue Disorders from 3D Aortic MR Images using Independent Component Analysis

---

Accepted for publication by CVAMIA'06 in Springer LNCS.

Michael Sass Hansen, Fei Zhao, Honghai Zhang, Nicholas E. Walker, Andreas Wahle, Thomas Scholz and Milan Sonka.

Abstract A computer-aided diagnosis (CAD) method is reported that allows the objective identification of subjects with connective tissue disorders from 3D aortic MR images using segmentation and independent component analysis (ICA). The first step to extend the model to 4D (3D + time) has also been taken. ICA is an effective tool for connective tissue disease detection in the presence of sparse data using prior knowledge to order the components, and the components can be inspected visually.

3D+time MR image data sets acquired from 31 normal and connective tissue disorder subjects at end-diastole (R-wave peak) and at 45% of the R-R interval were used to evaluate the performance of our method. The automated 3D segmentation result produced accurate aortic surfaces covering the aorta. The CAD method distinguished between normal and connective tissue disorder subjects with a classification accuracy of 93.5 %.

Appendix D

Detection of Connective Tissue Disorders from 4D Aortic MR Images using Independent Component Analysis

---

Submitted to MICCAI'06 , awaiting review.

Michael Sass Hansen, Fei Zhao, Honghai Zhang, Bjarne K. Ersbøll, Andreas Wahle, Thomas Scholz and Milan Sonka.

Abstract Independent component analysis (ICA) is applied in a computer-aided diagnosis (CAD) method that allows the objective identification of subjects with connective tissue disorder from 4D aortic MR images. A novel idea of time-invariant independent components assists in the disease detection in the presence of sparse data with high dimensionality. Prior knowledge of the source distribution is utilized using an appropiate ordering of the components.

4D MR image data sets acquired from 21 normal and 10 diseased subjects were used to evaluate the performance of our method. The automated 4D segmentation result produced accurate aortic surfaces. The CAD method distinguished between normal and diseased subjects with a classification accuracy of 96.8 %, using features showing correspondence to clinical observations of connective tissue disorder.

Bibliography

[1] *The Centers for Disease Control and Prevention (CDC).* http://www.cdc.gov/.

[2] Fei Zhao, Honghai Zhang, Nicholas E. Walker, Fuxing Yang, Mark E. Olszewski, Andreas Wahle, Thomas Scholz, and Milan Sonka. Quantitative analysis of two-phase 3D+time aortic MR images. *SPIE 2006*, Image Processing:not published yet, 2006.

[3] Joseph P. Hornak. The basics of MRI. *http://www.cis.rit.edu/htbooks/mri/*, 1996.

[4] Georg Freser Hans Engels. Magnetic resonance imaging and electromagnetic fields. *http://www.magres.nottingham.ac.uk/safety/eu/Frese_text.pdf*, 2003.

[5] Thomas B. Sheridan. An intelligent cardiopulmonary system for the home health market. *The Home Automation and Healthcare Consortium*, Progress Report No.2-3, 1999.

[6] N. Sondheimer. Marfan syndrome. *http://www.nlm.nih.gov/medlineplus/ency/article/000418.htm*, 2006.

[7] Inc. Merck & Co. Hereditary connective tissue disorders. *http://www.merck.com/mmhe/sec23/ch279/ch279a.html*, 2003.

[8] Characteristics (features) of marfan syndrome. *http://www.mayoclinic.org/marfan-syndrome/features.html*, 2004.

[9] The National Marfan Foundation. Pediatric concerns. *available at: http://www.marfan.org*, 2003.

[10] American Heart Association. Aortic aneurysm. *http://www.americanheart.org/presenter.jhtml?identifier=4455*, 2006.

[11] Cedar-Sinais Hospital. Aortic aneurysm. *http://www.csmc.edu/6203.html*, 2006.

[12] F. Arnaldo. Aortic dissection. *http://www.nlm.nih.gov/medlineplus/ency/ article/000181.htm*, 2006.

[13] Milan Sonka et al. Highly automated analysis of 4-d cardiavascular mr data. 2003.

[14] D. Rueckert, P. Burger, S. Forbat, R. Mohiaddin, and G. Yang. Automatic tracking of the aorta in cardiovascular MR images using deformable models. *IEEE Trans. on Medical Imaging*, 16(5):581–590, 1997.

[15] T. Behrens, K. Rohr, and H.S. Stiehl. Robust segmentation of tubular structures in 3D medical images by parametric object detection and tracking. *IEEE Trans. on Systems, Man, and Cybernetics*, 33(4):554–561, 2003.

[16] Marleen de Bruijne, Bram van Ginneken, Max A. Viergever, and Wiro J. Niessen. Adapting active shape models for 3D segmentation of tubular structures in medical images. In *Proceedings of IPMI'03*, pages 136–147, 2003.

[17] M. Subasic, S. Loncaric, and E. Sorantin. 3D image analysis of abdominal aortic aneurysm. In *Proceedings of SPIE'02*, pages 1681–1689, 2002.

[18] J. Hérault and B. Ans. Circuits neuronaux à synapses modifiable: décodage de messages composites par apprentisage non supervisé. *C. -R de l'Acad´mie des Sciences*, 299(III-13):525–528, 1984.

[19] A. Hyvärinen and E. Oja. A fast fixed-point algorithm for independent component analysis. *Neural Computation*, 9(7):1483–1492, 1997.

[20] Mehmet Üzümcü, Alejandro F. Frangi, Johan H.C. Reiber, and Boudewijn P.F. Lelieveldt. Independent component analysis in statistical shape models. *Proceeding of SPIE*, 5032:375–383, 2003.

[21] A. Suinesiaputra, A.F. Frangi, M. Üzümcü, J.H.C. Reiber, and B.P.F. Lelieveldt. Extraction of myocardial contractility patterns from short-axes mr images using independent component analysis. *CVAMIA 2004*, 2004.

[22] R. Malladi and J. A. Sethian. A real-time algorithm for medical shape recovery. In *Proceedings of ICCV '98*, pages 304–310, 1998.

[23] K. Palagyi, E. Sorantin, E. Balogh, A. Kuba, Cs. Halmai, B. Erdhelyi, and K. Hausegger. A sequential 3D thinning algorithm and its medical applications. In *Proceedings of IPMI'01*, pages 409 – 415, 2001.

[24] M. Unser, A. Aldroubi, and M. Eden. B-spline signal processing: Part I - theory. *IEEE Trans. on Signal Processing*, 41(2):821–833, 1993.

[25] M. Unser, A. Aldroubi, and M. Eden. B-spline signal processing: Part II - efficient design and applications. *IEEE Trans. on Signal Processing*, 41(2):834–848, 1993.

[26] M. Sonka, V. Hlavac, and R. Boyle. *Image Processing, Analysis, and Machine Vision.* PWS, 1998.

[27] M Sonka, G Reddy, and S M Collins. Adaptive approach to accurate analysis of small diameter vessels in cineangiograms. *Trans. on Medical Imaging*, 16(1):87–95, 1997.

[28] M Sonka, X Zhang, M Siebes, M S Bissing, S C DeJong, S M Collins, and C R McKay. Segmentation of intravascular ultrasound images: A knowledge-based approach. *Trans. on Medical Imaging*, 14(4):719–732, 1995.

[29] Steven Charles Mitchell. Active appearance model segmentation in medical image analysis. *PhD Thesis*, 2004.

[30] William E. Lorensen and Harvey E. Cline. Marching cubes: A high resolution 3D surface construction algorithm. In *Proceedings of SIGGRAPH '87*, volume 21(4), pages 163–169, 1987.

[31] Aapo Hyvärinen, Juha Karhunen, and Erkki Oja. Independent component analysis. *A volume in the Wiley series on Adaptive and Learning Systems for Signal Processing, Communications, and Control.*, pages 305–313, 2001.

[32] Aapo Hyvärinen. Survey on independent component analysis. *www.cis.hut.fi/ aapo/*, 1:1–35, 2001.

[33] N. Delfosse and P. Loubaton. Adaptive blind separation of independent sources: a deflation approach. *Signal Processing*, 45:59–83, 1995.

[34] Antoine Souloumiac JeanFrancois Cardoso. Blind beamforming for non-gaussian signals. *IEE ProceedingsF*, 140 No. 6:362–370, 1993.

[35] Kun Zhang and Lai-Wan Chan. Dimension reduction based on orthogonality - a decorrelation method in ica. *Artificial Neural Networks and Neural Information Processing - ICANN/ICONIP 2003*, LNCS 2714:132–139, 2003.

[36] Bjarne Erbøll and Knut Conradsen. *An introduction to statistics, Volume 2.* Department of Informatics and Mathematical Modelling., 2003.

[37] Richard O. Duda, Peter E. Hart, and David G. Stork. *Pattern Classification.* John Wiley and sons inc., 2001.

[38] Will Schroeder, Ken Martin, and Bill Lorensen. *The Visualization Toolkit, 3rd Edition.* Kitware, inc., 2004.

[39] Lisa S. Avila et al. *The VTK User's Guide.* Kitware, inc., 2004.